Constraints on the timing of late-Eburnean metamorphism, gold mineralisation and regional exhumation at Damang mine, Ghana

Alistair White[a,b], Ray Burgess[c], Norman Charnley[a], David Selby[d], Martin Whitehouse[e], Laurence Robb[a], David Waters[a],

[a]Department of Earth Sciences, University of Oxford, South Parks Road, Oxford, OX1 3AN, UK

[b]CSIRO Earth Science and Resource Engineering, Australian Resources Research Centre, 26 Dick Perry Avenue, Kensington, WA 6151, Australia

[c]School of Earth, Atmospheric and Environmental Sciences, University of Manchester, Williamson Building, Oxford Road, Manchester, M13 9PL, UK

[d]Department of Earth Sciences, Durham University, Science Labs, Durham, DH1 3LE, UK

[e]Laboratory for Isotope Geology, Swedish Museum of Natural History, Box 50 007, SE-104 05 Stockholm, Sweden

Corresponding author e-mail address: Alistair.White@csiro.au

Postal address: CSIRO, PO Box 1130, Bentley, WA 6102, Australia

Tel.: +61 8 6436 8735, Fax: +61 8 6436 8555

Other author e-mail contacts:

ray.burgess@manchester.ac.uk, norman.charnley@earth.ox.ac.uk, david.selby@durham.ac.uk, martin.whitehouse@nrm.se, dave.waters@earth.ox.ac.uk, laurence.robb@earth.ox.ac.uk

ABSTRACT

The Damang gold deposit in southwest Ghana is unique among known deposits in Ghana, comprising gold mineralisation in two distinct styles. Early gold hosted in a stratigraphically controlled, auriferous quartz-pebble conglomerate horizon is overprinted by later mineralisation contained in a sub-horizontal fault-fracture quartz vein array. A multi-system geochronological study is used to constrain the timing of igneous activity, regional metamorphism, gold mineralisation and the thermal history at Damang. U/Pb analysis of zircons from Birimian volcaniclastic and intrusive rocks constrain volcanism and associated intrusive activity at 2178.0±9.3 Ma and 2164.6±8.0 Ma respectively, which is consistent with previous studies. The age of formation of staurolite-grade, amphibolite facies peak metamorphic mineral assemblages at 2005±26 Ma is provided by U-Th-total Pb EPMA analysis of metamorphic monazite grains in the Tarkwa Phyllite. Measured $^{40}Ar/^{39}Ar$ biotite ages range between 1980±9 Ma and 1882±9 Ma. Argon diffusion modelling with the program DIFFARG suggests that this age range could be achieved by a period of rapid cooling, at a rate of approximately 17ºC/Ma, followed by a prolonged period of much slower cooling, at a rate of 0.15ºC/Ma. The period of rapid cooling is interpreted to represent localised exhumation of the Damang host rocks during the latest stage of the Eburnean orogeny at the time of hydrothermal gold mineralisation. Given these age constraints, hydrothermal gold mineralisation is inferred to have occurred between approximately 2030 Ma and 1980 Ma. These ages constrain metamorphism, fluid flow and gold mineralisation at Damang and are the youngest currently recognised in the Birimian of SW Ghana.

Keywords: Birimian; Ghana; Eburnean; U/Pb dating; U-Th-Total Pb dating; Ar/Ar dating

Highlights:

- A multi-system geochronological study of the Damang deposit is presented.
- Birimian volcanism and intrusive activity is consistent with previous studies.
- Ages for regional peak metamorphism and cooling are the youngest recorded in the Birimian of SW Ghana.
- Ar diffusion modelling suggests exhumation at the time of gold mineralisation.

1. Introduction

The Paleoproterozoic Birimian terrane of Ghana is a gold province of global importance, hosting numerous world-class shear zone-hosted, hydrothermal (e.g. Obuasi) and paleoplacer-style (e.g. Tarkwa) gold deposits. Gold mineralisation occurred during the 2130 to 1980 Ma Birimian orogeny, known elsewhere in Africa as the Eburnean orogeny (Eisenlohr and Hirdes, 1992; Feybesse and Milési, 1994; Allibone et al., 2002; Hirdes and Davis, 2002; Feybesse et al., 2006; Harcouët et al., 2007). Earlier deformation events have also been described, termed the 'Eoeburnean' in Ghana (de Kock et al., 2011; Perrouty et al., 2012) and the Tangaean in neighbouring Burkina Faso (Hein, 2010). Placer gold deposition occurred early in the orogenic cycle, during sedimentation of the Tarkwaian System (Milési et al., 1991). In contrast, orogenic gold deposits formed later, post-dating peak regional metamorphism (Milési et al., 1991; Eisenlohr, 1992).

The Damang deposit is unique among known gold deposits in Ghana. Here, gold is hosted in a stratigraphically controlled, auriferous quartz-pebble conglomerate, as at neighbouring Tarkwa mine, and then overprinted by later orogenic gold mineralisation contained in a sub-horizontal fault-fracture quartz vein array (Pigois et al., 2003; Tunks et al., 2004). Given the apparently unique structural setting of hydrothermal mineralisation at Damang, it remains unclear how this deposit relates to the regional geodynamic framework, the most recent and comprehensive interpretation of which is given by Perrouty et al. (2012). Furthermore, a greater understanding of the Damang deposit is vital from a regional exploration perspective by defining additional geological domains that are prospective for gold mineralisation.

As with many hydrothermal mineral deposits, the Damang region has undergone numerous distinct igneous, metamorphic, mineralising and tectonic events. Thus, a multi-system geochronological approach is required to constrain the timing of the different episodes. In this paper, we present the results of U/Pb zircon dating of Birimian basement igneous rocks, U-Th-total Pb analysis of metamorphic monazite from a metapelitic unit, the Tarkwa Phyllite, Re/Os dating of gold-associated sulphide phases and $^{40}Ar/^{39}Ar$ analysis of metamorphic and hydrothermal biotite from a range of lithologies. These data are used to provide an interpretation of the timing of the Damang deposit in a regional context.

2. Regional geologic setting and geochronological framework

Ghana lies on the southern margin of the Archean-Paleoproterozoic Man Shield of West Africa (Ennih and Liégeois, 2008). The western portion of Ghana contains the Paleoproterozoic Birimian terrane, which comprises a number of sub-parallel, NE–SW-trending, several hundred kilometre long, linear volcano-sedimentary greenstone belts, with intervening sedimentary basins (Fig. 1A). The belts are primarily composed of basic to intermediate volcanics with associated volcaniclastic deposits (Leube et al., 1990), formed during a 2.1 to 2.0 Ga phase of crustal growth (Abouchami et al., 1990; Boher et al., 1992). Trace element geochemistry suggests a combination of back-arc basin LREE-depleted tholeiites and subduction zone-related calc-alkaline rocks (Dampare et al., 2008). Clastic sediments of the Tarkwaian System occasionally overly the volcanic belts (Davis et al., 1994; Pigois et al., 2003). These sediments comprise a broadly upward-fining sequence of clastic sediments interpreted as infill of a tensional rift basin (Ledru et al., 1994). The Tarkwaian System hosts widespread synsedimentary, paleoplacer-type deposits hosted in quartz-pebble conglomerate horizons, which are derived from an as yet unknown pre-Eburnean source (Milési et al., 1991; Eisenlohr, 1992; Pigois et al., 2003). The large basins between the volcanic belts comprise voluminous volcaniclastic, clastic sedimentary, and chemical sedimentary rocks that are interpreted to be lateral facies equivalents of the volcanic belts (Leube et al., 1990). Along the basin margins, belt volcanic and basin sediments are intercalated and interpreted as representing coeval formation of oceanic basins between a series of volcanic arcs (Leube et al., 1990).

Both belts and basins are intruded by two series of granitic plutons, the older belt-type and younger basin-type granitoids respectively (Hirdes et al., 1992; Taylor et al., 1992; Oberthür et al., 1998). The belt-type granitoids range in composition from hornblende- and biotite-bearing granites to diorite, monzogranites, syenites and even tonalities and trondhjemites (Leube et al., 1990; Eisenlohr and Hirdes, 1992; Hirdes et al., 1992). Individual plutons often form composite batholiths comprising several different granitoid types. Plagioclase megacrysts are common and are typically heavily saussuritised or sericitised, which has been used to suggest that the rocks have been subjected to regional metamorphism and/or hydrothermal alteration (Eisenlohr and Hirdes, 1992). The lack of any observable metamorphic aureole may also be related to overprinting by regional metamorphism. Xenoliths of basalt are common and in places there is a gradational transition between coarse-grained granitoid and basalt. Based on this observation, Eisenlohr and Hirdes (1992) suggest a close genetic relationship between the belt-type granitoids and the Birimian volcanics during a common magmatic event. The basin-type granitoids intrude the Birimian sedimentary basins as large batholiths surrounded by extensive metamorphic aureoles. They are predominantly two-mica granitoids with lesser biotite-only or hornblende-only types. They are typically granodioritic in composition but range from granite to monzogranite or tonalite (Leube et al., 1990; Eisenlohr and Hirdes, 1992). The basin-type granitoids are extensively foliated, with fabric development interpreted to be synchronous with regional deformation (Eisenlohr and Hirdes, 1992).

Deformation, metamorphism and gold mineralisation occurred during the 2130 to 1980 Ma Eburnean orogeny (Eisenlohr and Hirdes, 1992; Feybesse and Milési, 1994; Feybesse et al., 2006; Perrouty et al., 2012). Deformation likely occurred during continuous progressive, broadly northwest – southeast compression (Eisenlohr and Hirdes, 1992; Feybesse and Milési, 1994). Regional metamorphism is typically quoted as 'low-grade', especially with regard to the Tarkwaian System, with metabasites containing mineral assemblages up to greenschist facies. Higher-grade garnet and kyanite bearing assemblages have been recorded in aureoles to large granitoid plutons (Leube et al., 1990; Eisenlohr and Hirdes, 1992; Milési et al., 1992; Ledru et al., 1994; Mumin and Fleet, 1995), while more detailed metamorphic studies have highlighted widespread occurrences of amphibolite facies rocks, with peak conditions of 500-600ºC and 4-6 kbar (John et al., 1999; Klemd et al., 2002; White et al., 2013).

Orogenic gold mineralisation typically occurs late in the orogenic cycle and is contained in regional-scale, sub-vertical shear zones along the margins of the

Birimian belts (Leube et al., 1990; Milési et al., 1991; Oberthür et al., 1997). In these shear zones, gold is contained within steeply dipping quartz veins and in massive disseminated sulphide deposits (Oberthür et al., 1997; Allibone et al., 2002). These deposits share many characteristics with Archean greenstone-hosted gold deposits such as those of the Yilgarn craton in Western Australia (Goldfarb et al., 2001; 2005), although they have also been categorised as turbidite-hosted deposits due to the high proportion of volcaniclastic and sedimentary material in the host rocks (Berge, 2011). Within Ghana, orogenic gold deposits of varying sizes are known from all Birimian belts. The largest and greatest numbers of deposits occur along the northwest margin of the Ashanti belt. Fluid inclusion, mineral thermometry and thermodynamic modelling techniques suggest a spread of formation temperatures and pressures for Ghanaian orogenic gold deposits, typically in the range 300-450ºC and 2-5 kbar, with a dominantly low salinity, CO_2-rich fluid (Mumin et al., 1996; Schmidt Mumm et al., 1997; Yao et al., 2001; Wille and Klemd, 2004; White et al., 2013).

2.1 Existing geochronology in Ghana

The Birimian terrane has been the subject of a number of geochronological studies, particularly during the 1990s. A comprehensive discussion of the current geochronological understanding in Ghana is given by Perrouty et al. (2012) and summarised here. Quoted uncertainties in this section are 2σ unless otherwise stated. The small number of U/Pb zircon ages for Birimian volcanism range from as old as 2266±2 Ma to as young as 2158±5 Ma (Hirdes and Davis, 1998; Loh et al., 1999; Feybesse et al., 2006). The maximum age of Birimian sedimentation in the Kumasi basin is constrained by detrital zircons, giving ages of 2135±5 Ma (Davis et al., 1994) and 2154±2 (1σ) Ma (Oberthür et al., 1998).

Significantly more data are available for the belt- and basin-type granitoids in Ghana. The older belt-type granitoids intruded the Birimian belt volcanics between 2200±4 Ma and 2151±7 Ma (Hirdes et al., 1992; Oberthür et al., 1998; Feybesse et al., 2006; Brownscombe, 2009), with the majority falling in the range 2179 – 2172 Ma. This overlap with Birimian mafic volcanism suggests a comagmatic origin. Peak metamorphism in the belt-type granitoids is estimated to have occurred at 2092±2 (1σ) Ma based on a U/Pb titanite age provided by Oberthür et al. (1998). The basin-type granitoids are typically younger than the belt-type granitoids with intrusion ages between 2116±2 and 2088±1 (1σ) Ma, and are likely related to crustal thickening and melting during the Eburnean orogeny (Hirdes et al., 1992; Davis et al., 1994; Oberthür et al., 1998; Brownscombe, 2009). Metamorphism was at a similar time to the basin-type granitoids, with a U/Pb titanite age of 2086±4 (1σ) Ma reported by Oberthür et al. (1998).

Detrital zircon studies constrain the maximum age of Tarkwaian sedimentation to around 2132±3 Ma (Davis et al., 1994) and 2133±4 Ma (Pigois et al., 2003). A minimum age constraint is provided by the intrusion of the Banso granite, in the northern Ashanti belt, with a Pb/Pb titanite age of 2097±2 (1σ) Ma (Oberthür et al., 1998).

Estimates of the timing of orogenic gold mineralisation are mostly determined indirectly, based on metamorphic/hydrothermal minerals, such as rutile (2086±4 (1σ)

Ma, Oberthür et al., 1998) or xenotime (2063±9 Ma, Pigois et al., 2003). These are the youngest ages determined in the Birimian terrane of Ghana, post-dating all lithological units as well as being marginally younger than the best estimate for regional peak metamorphism at 2092±2 (1σ) Ma (Oberthür et al., 1998).

2.2 Geology of the Damang deposit

The Tarkwa-Damang region is folded into a series of NE-orientated and NNE- to NE-plunging anticlines and synclines. The Damang gold mines and associated satellite deposits occur along both the east and west limbs of the Damang anticline, with the majority of hydrothermal mineralisation present on the western limb (Fig. 1B). All known gold mineralization is hosted within Tarkwaian System sediments, which uncomformably overlie, or are faulted against, Birimian volcanic and volcaniclastic rocks in the core of the anticline. The Birimian volcanic rocks are intruded by numerous small bodies of a phaneritic quartz diorite, termed the Diorite Porphyry. This is encountered predominantly along the contact between the Birimian and Tarkwaian rocks, although its age, and therefore relationship to the country rocks, is currently unknown. A post-Tarkwaian age of intrusion could have profound implications for the source of mineralizing fluids and/or heat generation driving their circulation. This issue is addressed in this paper.

The Tarkwaian System comprises a predominantly upward-fining sequence of clastic sediments (Fig. 1C). The barren Kawere Group at the base of the Tarkwaian system comprises a coarse pebble-boulder conglomerate that fines upwards to coarse sandstone. The economically important arenaceous Banket Series overlies the Kawere

Group and is made up of cross- to planar-bedded quartzite and arkose. The Banket Series hosts all paleoplacer-style gold mineralisation in four quartz-lithic conglomerate horizons within which gold is associated with other heavy minerals along bedding planes and cross-bedded foresets. The Banket Series is also the major host to hydrothermal mineralisation. The overlying Tarkwa Phyllite is a finely laminated metapelite with a well-developed mid-amphibolite facies mineral assemblage (White et al., 2013). The uppermost unit of the Tarkwaian System is the Huni Sandstone, a thick sequence of massive feldspathic sandstones, which is poorly mineralised. Mafic dykes and sills intrude the upper portions of the Tarkwaian stratigraphy. These intrusions range in composition from gabbro to diorite and are now uniformly overprinted with an amphibolite facies hornblende-plagioclase dominated assemblage (White et al., 2013).

Detailed structural mapping and analysis by Tunks et al. (2004) identified four major phases of deformation, termed TD_1 to TD_4. TD_1 created the macroscopic, upright, NE-trending folds and associated NE-trending faults, including the Damang fault, during NW-SE compression. This corresponds to regional event D3 of Perrouty et al. (2012) and forms the first-order control on later hydrothermal mineralisation. Microstructures within the Damang fault zone indicate that motion on the fault occurred between biotite and garnet growth in the Tarkwa Phyllite during prograde metamorphism (White, 2011). TD_2 is represented by numerous ENE-trending thrust faults and minor ENE-trending folds, formed during NNW-SSE compression. TD_3 WNW-ESE compression post-dated peak regional metamorphism and primarily resulted in the extensive sub-horizontal, extensional, brittle fault-fracture mesh, which contains gold-bearing quartz veins (Fig. 2). TD_3 corresponds to regional event D6 of

Perrouty et al. (2012). The final TD_4 event produced minor, brittle strike-slip faulting, often along pre-existing fault surfaces.

Thermodynamic modelling of metamorphic mineral assemblages estimates peak metamorphic conditions at around 590ºC and 5.5 kbar (White et al., 2013). Hydrothermal alteration and associated gold mineralisation occurred later, under much lower grade conditions in the range of 400-450ºC and 1-2 kbar, and overprint the earlier regional metamorphic assemblages (White et al., 2013).

3. Samples

The successive geologic events considered to have affected the Damang region, including igneous activity, metamorphism and mineralisation, are recorded by the growth of different minerals that are amenable to age determinations using a range of different isotopic dating techniques. Therefore, a multi-system approach is required to fully constrain the timing of these different processes (Table 1). Analytical methods applied to each technique are described in Appendix 1. Although Re/Os analysis of gold-associated sulphide phases was attempted, it was ultimately unsuccessful at providing any meaningful age constraint. Details and results of this work are available in online supplementary material S1 with a short summary discussion given below.

3.1 U/Pb zircon analysis

The volcanic rocks of the intrusive Diorite Porphyry and the Birimian volcaniclastic basement contain abundant zircon and are ideally suited to a geochronological study. As described in section 2.2, the Diorite Porphyry is not well constrained within the geological history at Damang and determining an age of intrusion is vital. In order to place any age calculated for the Diorite Porphyry in context, a Birimian volcaniclastic unit has also been analysed.

The Diorite Porphyry (sample AWADi) is a coarse-grained quartz-diorite comprising an igneous texture of coarse biotite amongst randomly orientated, interlocking plagioclase feldspar laths, with lesser quartz and minor chlorite, ankerite and ilmenite (Fig. 3A-C). The Birimian volcaniclastic rock (sample AWABv) is a fine- to medium-grained, massive rock with a matrix of quartz, lesser feldspar, muscovite, very fine chlorite flakes and trace ilmenite, all overprinted by coarse biotite flakes (Fig. 3D-F). Both of these samples are typical of their respective units across the Damang region.

3.2 U-Th-Total Pb monazite analysis

Monazite is abundant in samples of the Tarkwa Phyllite. Suggested pressure-temperature conditions of monazite producing reactions include during garnet-grade (Catlos et al., 2001), staurolite-in (Kohn and Malloy, 2004) and aluminosilicate-in (Wing et al., 2003) prograde reactions, or hydrothermal processes (Townsend et al., 2000). Additionally, there are many recorded occurrences of detrital monazites remaining stable through low-grade metamorphism up to higher grade conditions (Parrish, 1990; Suzuki et al., 1994). Recent studies suggest that rare earth elements in metamorphic rocks are hosted in monazite at very low metamorphic grades, often as detrital grains, in allanite at moderate grades and eventually as new-formed monazite at the highest grades (Janots et al., 2008; Rasmussen and Muhling, 2009; Spear, 2010). The formation of metamorphic monazite is therefore intimately associated with the breakdown of allanite, which typically occurs close to, but ultimately independent of, the staurolite-in isograd (Tomkins and Pattison, 2007; Corrie and Kohn, 2008; Janots et al., 2008). Peak metamorphic mineral assemblages in the Tarkwa Phyllite clearly show that the Damang region reached staurolite grade metamorphic conditions (White et al., 2013). This implies that monazite growth occurred at or very close to peak metamorphism and their age is therefore a good estimate of these conditions.

Monazite grains in the Tarkwa Phyllite are generally subhedral and all occur in the same petrographic setting; as matrix phases, interstitial amongst quartz, plagioclase and muscovite (Fig. 4). Backscattered electron imaging indicates that the grains are homogeneous and do not contain distinct cores or overgrowths. All monazites are interpreted to have had the same growth history during a single growth event. In mineralised rocks, all monazite grains are highly altered and surrounded by an irregular, broadly concentric domain of apatite-allanite-epidote (Fig.4E). This phenomenon was studied in detail by Finger et al. (1998) and Upadhyay and Pruseth (2012), with similar reaction textures noted by Dini et al. (2004) and Rasmussen and Muhling (2009). Finger et al. (1998) and Upadhyay and Pruseth (2012) suggested that the inner apatite zone is a direct replacement of monazite, with the displaced REEs forming the surrounding allanite corona (Fig. 4F). However, Upadhyay and Pruseth (2012) also state that the allanite zone could be a pseudomorphic replacement. Both groups also describe a chemical mass balance that suggests breakdown initiated by an influx of hydrothermal Ca, Fe, Si and Al. This agrees in principle with Spear (2010), whose thermodynamic calculations suggest the monazite-allanite transition is a function of the host CaO (and Al_2O_3) content, with higher Ca-contents favouring allanite stability. Ultimately, these reaction textures support the assertion that the monazite is metamorphic in origin and not related to a hydrothermal event since the mineralisation process is, in this case, monazite-destructive (Fig. 4). Importantly, both Finger et al. (1998) and Upadhyay and Pruseth (2012) suggested that relic monazite grains preserve their U-Th-Pb characteristics and are, therefore, still viable chronometers of the pre-mineralisation metamorphic history.

Although the Tarkwa Phyllite contains numerous monazite grains, their small size (typically 10-20 μm) precludes analysis by ion probe techniques. Instead, U-Th-total Pb dating using an electron probe microanalyser (EPMA) was utilised. Full descriptions of the principles, applications and limitations of this technique are given by Suzuki and Adachi (1991), Suzuki et al. (1991), Montel et al. (1996), Cocherie et al. (1998), Scherrer et al. (2000), Williams and Jercinovic (2002), Lisowiec (2006) and Spear et al. (2009). Monazite is a suitable mineral for EPMA U-Th-total Pb analysis as it commonly contains several weight percent ThO_2 and hundreds of ppm to a few weight percent UO_2, leading to rapid accumulation of radiogenic Pb, while rarely containing common Pb exceeding 1 ppm (Parrish, 1990). Unlike isotopic methods, chemical dating is unable to detect discordant monazites, which would produce geologically meaningless ages. However, monazites typically are concordant, which reduces this concern (Cocherie et al., 1998; Scherrer et al., 2000). Additionally, a number of studies have investigated the behaviour of Pb in monazite and while diffusion and loss can occur, it is generally uncommon and not thought to be a major problem (Suzuki et al, 1994; Montel et al., 1996; Cocherie et al., 1998).

3.3 $^{40}Ar/^{39}Ar$ biotite analysis

Biotite is abundant in a range of lithologies at Damang, occurring as a metamorphic phase in the sedimentary rocks, particularly the Tarkwa Phyllite, and as a major phase in gold-bearing, hydrothermally altered dolerite intrusives (Fig. 5). In this latter case, biotite is a product of the potassic-sulphidation-carbonation alteration that occurred during gold deposition (White et al., 2010; White et al. 2013). Biotite also occasionally occurs within gold-bearing quartz veins themselves (Fig. 5A). Grain size and texture varies between samples from coarse, well-crystallised crystals to fine, poorly formed flakes. The former type was selected for analysis. The commonly quoted Ar closure temperature for biotite is approximately 300°C (McDougall and Harrison, 1999), which is lower than the estimated conditions of gold mineralisation (375 – 425°C) at Damang (White et al., 2013), thereby allowing a post-mineralisation (and therefore post-metamorphic) cooling history to be determined. Consequently, any $^{40}Ar/^{39}Ar$ ages place a minimum age constraint on the gold mineralisation event.

Six individual samples were analysed, covering all parageneses. One sample of very coarse grained biotite from within a massive quartz vein was divided into three aliquots. Other samples include regional metamorphic biotite in the Tarkwa Phyllite, igneous biotite in the Diorite Porphyry and Birimian volcaniclastic rocks, and hydrothermal biotite in altered dolerite. The Birimian volcaniclastic sample is more highly deformed than the others, with a well-developed crenulation cleavage formed during pre-Tarkwaian deformation (White, 2011).

4. Results

4.1 U/Pb

4.1.1 Birimian Volcaniclastic

Birimian Volcaniclastic sample AWABv contains euhedral zircons that show extensive zoning, with many exhibiting distinct core and rim domains (Fig. 6A). Eighteen individual zircon grains were selected for analysis including 3 grains with core and rim zones, giving a total of 21 analysis points. Eight of these are discordant while the remaining 13 concordant zircon grains indicate a maximum formation age of 2178.0±9.3 Ma (2σ, MSWD=1.8) (Fig. 7A). The core domains produce no discernible difference in age and are therefore not xenocrystic, but are instead interpreted to represent a short break in growth conditions and/or a change in magma system dynamics. Tabulated results are given in Table 2.

4.1.2 Diorite Porphyry

The Diorite Porphyry, sample AWADi, contains zircons that are highly cracked and contain numerous large inclusions. Zircons considered suitable for analysis are largely homogeneous with little compositional zoning (Fig. 6B). A total of 14 zircon grains were selected for analysis. Four of these are strongly discordant and fall along a straight-line discordia that passes within error of the origin of the plot. This Pb-loss is likely related to recent uplift and/or near-surface weathering and these grains are therefore discounted. The remaining 10 concordant zircon grains indicate an age of formation of 2164.6±8.0 Ma (2σ, MSWD=1.6) (Fig. 7B, Table 2), consistent with intrusion into the Birimian volcaniclastic rocks.

4.2 U-Th-Total Pb

The final calculation of a monazite U-Th-total Pb age is best conducted using repeated measurements of a single, homogeneous domain (Williams and Jercinovic, 2002). Since the size of monazite grains in this study are such that only one analysis spot can be placed on each grain, this translates to making measurements of a homogeneous population. The REE, U, Th, Si and Ca contents of all analysed monazite grains are plotted in Figure 8. Despite a small degree of scatter, all three samples are compositionally uniform and indistinguishable. All monazites can therefore be treated as a single homogeneous population (Williams and Jercinovic, 2002).

The final age and uncertainty for the 53 analysed monazite grains is 2005±26 Ma (95% C.I., MSWD = 2.1), which is shown using the histogram approach of Montel et al. (1996) in Figure 9A. The total probability histogram (the thick line in Figure 9A) defines a function that may be fitted to two sub-populations. However, as discussed above, there is no petrographic or geochemical basis on which to define two separate populations, and also, therefore, no statistical significance to defining two age groups. Results are presented according to the isochron method of Suzuki and Adachi (1991) (Fig. 9B), although this technique was not used to calculate the final age. Finally, a weighted average approach calculated in Isoplot/Ex v.3.7 (Ludwig, 2003) is shown in Figure 9C. Tabulated results are presented in Table 3.

4.3 $^{40}Ar/^{39}Ar$

Composition, particularly X(Mg) (Mg/ (Fe + Mg)), has been suggested to have an effect on Ar retention in biotite, and consequently an effect on the calculated ^{40}Ar/^{39}Ar age (Harrison et al., 1985; Grove and Harrison, 1996). Therefore, it is important to know the compositions of biotites within a sample prior to ^{40}Ar/^{39}Ar analysis. The compositions of biotite grains from samples analysed for ^{40}Ar/^{39}Ar are shown in Fig. 10. Averaged compositions for each sample are given in Table 4, with the complete data set in online supplementary material S2. Biotite compositions for samples TpArBt1, DoArBt2 and AWDDo6 are taken from accompanying petrographic samples AWDP1, AWDDo1 and AWDDo4 respectively. These petrographic samples were collected from the same pit location or drill core and depth as the ^{40}Ar/^{39}Ar samples. No compositional data are available for sample DoArBt4, although they are not expected to be different to other dolerite samples. The majority of analyses have X(Mg) values in the range 0.45 – 0.55. Samples of the Birimian basement, AWADi1 and AWABv1, have slightly lower X(Mg) values (0.45 – 0.50) than samples from the Tarkwaian System, AWDP1, AWDDo1 and AWDDO1 (0.52 – 0.56). This variation is not significant given the variability within a given sample. Sample AWDDo4 shows the greatest variability with X(Mg) values up to 0.65.

All 8 analysed samples produce extremely well-defined step-heating plateaux (Fig. 11), although there is a broad spread in the resulting ages, covering some 100 Ma. The step-heating plateau for each sample is shown in Figure 11 along with its final age, uncertainty at the 2σ level, the number of heating steps that define the plateau and the percentage of released ^{39}Ar that constitutes the plateau. Tabulated results are presented in Table 5.

Samples DoArBt4, DoArBt4-2 and DoArBt4-3 are aliquots from a single sample and produce consistent ages. Sample DoArBt4 gives an age of 1980±9 Ma (2σ, 13 steps, 97% of released ^{39}Ar). Sample DoArBt4-2 produced an age of 1973±9 Ma (2σ, 15 steps, 92% of released ^{39}Ar). Sample DoArBt4-3 produced an age of 1975±9 Ma (2σ, 13 steps, 98% of released ^{39}Ar).

The step heating plateau for sample DoArBt2 produces an age of 1927±9 Ma (2σ, 11 steps, 91% of released ^{39}Ar). Ca/K ratios for the low temperature steps, particularly around 700ºC, are high, indicating contamination of the sample by a mineral other than biotite. Given the relatively low temperature release of Ca-derived ^{37}Ar, this is interpreted to be carbonate, which is abundant in hydrothermal alteration zones and is often intimately associated with biotite (White et al., 2010, White et al., 2013). The higher temperature steps, however, typically have much lower Ca/K ratios with a high proportion of radiogenic ^{40}Ar and are therefore deemed to reliably represent Ar release from biotite.

The step-heating plateau for sample AWDDo6 gives an age of 1921±10 Ma (2σ, 5 steps, 89% of released ^{39}Ar). This age agrees well with sample DoArBt2. The low number of heating steps compared to other samples is due to the sample containing a very much lower proportion of Ar overall. As with sample DoArBt2, Ca/K ratios are high for the low temperature steps. The low total Ar and high Ca/K ratios are again interpreted to represent carbonate contamination. Similarly, the higher temperature steps have much lower Ca/K ratios with a high proportion of radiogenic ^{40}Ar and are therefore also deemed to reliably represent Ar release from biotite.

Sample TpArBt1 produced a step-heating plateau that gives an age of 1946±9 Ma (2σ, 11 steps, 90% of released ^{39}Ar). Sample AWABv1 produces a step-heating plateau that increases in age slightly as gas is released. Despite this, the plateau produces an age of 1898±11 Ma (2σ, 9 steps, 62% of released ^{39}Ar), which is distinctly younger than all other samples. The step-heating plateau for sample DiArBt1 produces an age of 1942±9 Ma (2σ, 11 steps, 82.3% of released ^{39}Ar).

5. Discussion

The U/Pb zircon age of 2178.0±9.3 Ma for the Birimian volcaniclastic is in good agreement with existing data for Birimian volcanism elsewhere in Ghana (Hirdes and Davis, 1998; Loh et al., 1999; Feybesse et al., 2006). The Diorite Porphyry intrusion produces a U/Pb zircon age of 2164.6±8.0 Ma. It is therefore interpreted as Birimian in age and was intruded in to the Birimian Supergroup prior to deposition of the Tarkwaian System. This age implies that the Diorite Porphyry is akin to the Belt-type granitoids and precludes the possibility of it being either a direct source of fluids, or a modifying influence on the later hydrothermal gold mineralisation.

U-Th-total Pb chemical dating of monazite in the Tarkwa Phyllite places peak regional metamorphism at 2005±26 Ma. This is more than 50 Ma younger than previous estimates of regional metamorphism obtained elsewhere in Ghana (c.f. section 2). It is also younger than the only published age for hydrothermal gold mineralisation at Damang of 2063±9 Ma, based on xenotime within gold-associated, hydrothermally altered rocks (Pigois et al., 2003). In this regard, it should be noted that unmineralised samples of the Tarkwa Phyllite, and other lithologies, occasionally also contain occurrences of xenotime, suggesting that xenotime may have an origin other than exclusively during the gold mineralizing event. Furthermore, Pigois et al. (2003) used the isocon method to demonstrate an increase in Y associated with hydrothermally altered Banket Series quartzites, which they then use to explain the growth of hydrothermal xenotime. However, Y and other heavy elements are most abundant in phases, such as xenotime, that occur along bedding planes and cross-bedded foresets. The distribution of such elements is therefore highly heterogeneous at a range of scales and as such we find that the Banket Series quartzites are unreliable for the construction of isocons. Ultimately, the age provided by Pigois et al. (2003), while reliably representing the age of xenotime growth, may not be indicative of hydrothermal alteration, and consequently gold mineralisation.

Details and results of Re/Os analysis of pyrite and pyrrhotite is presented in online supplementary material S1. Re/Os analysis did not produce a meaningful age due to a large degree of scatter in the data. The poor age constraint is a common problem in many sulphide systems and has certainly seriously affected some of the samples in this study. Furthermore, the diffusion of Os in pyrrhotite is significantly greater than for pyrite, resulting in pyrrhotite crystals commonly being isotopically reset (Brenan et al., 2000; Morelli, 2008). Similarly, sulphide minerals, particularly pyrrhotite, are known to gain or lose Re. Finally, sulphides can develop internal heterogeneity of isotope ratios, without requiring actual loss of either Re or Os (Barra et al., 2003; Cardon et al., 2008). The effect of this is that very large crystals, which are common at Damang, become broken up and not completely sampled during the sample preparation and isotope separation stages, such that a true isotopic ratio is not obtained. Many of these issues may be compounded by the association of both pyrite and pyrrhotite together in certain samples. Although the Re-Os age given here is imprecise and ultimately provides no useful constraint on the timing of gold mineralisation at the Damang deposit, the data ultimately imply that Damang's post-mineralization history was far from steady-state and was subject to processes that significantly disrupted the Re-Os systematics.

The $^{40}Ar/^{39}Ar$ results presented here cover a wide range of ages, from 1980±9 Ma to 1898±11 Ma, with no identifiable correlation to biotite paragenesis. This age range is consistently younger than the $^{40}Ar/^{39}Ar$ ages of 2029±4 Ma and 2034±4 Ma given by Pigois et al. (2003) for samples from Damang. The two ages presented by Pigois et al. (2003) were determined from aliquots of the same sample and, while they are internally consistent, the accuracy of these data has not been verified with other samples. Furthermore, the step-heating plateaux measured by Pigois et al. (2003) are more disturbed and less flat than those presented in this study. They are therefore initially excluded from consideration, although a discussion of this discrepancy is given below.

Given the close spatial distribution of the samples used in this study, it is unrealistic to suggest that the measured ages record a true variation in the timing of cooling through the same closure temperature. It is interpreted therefore, that this spread of ages is related to different closure temperatures for each sample. As such, an opportunity exists to extract a cooling history for the Damang region through the use of numerical modelling. Dodson's (1973) expression for closure temperatures in minerals is given by:

$$T = \frac{E/R}{\ln\left(A\tau\, D_0/r^2\right)} \quad (1)$$

Where E is activation energy, R is the gas constant, A is a geometric term related to model crystal structure, D_0 is the pre-exponent term in the Arrhenius relationship for the diffusion coefficient, r is grain radius and τ contains the cooling rate in the form:

$$\tau = \frac{-RT^2}{E\, dT/dt} \quad (2)$$

Since only biotites were analysed and the cooling rate is assumed to be common to all samples, the only variable capable of controlling T, according to this equation, is grain radius (r). For small grains, the volume over which Ar can diffuse is the same as the grain size and there exists a linear relationship between closure temperature and grain size (Wright et al., 1991; Markley et al., 2002; Alexandre, 2011). However, for larger grains above a radius of around 250 µm, these studies showed that this relationship breaks down, suggesting a limit to, or heterogeneity of the diffusion volume (Phillips and Onstott, 1988) and implying that larger grains can also lose Ar by other multipath mechanisms (Lee, 1995). In contrast, other studies have shown the age-grain size relationship continues to larger grains sizes of over 500 µm, up to macroscopic grain scale (Onstott et al., 1991; Hess et al., 1993; Hodges et al., 1994). More recent ideas regarding this apparent discrepancy include the role of mechanical deformation of grains, which serves to reduce the effective diffusion volume while not affecting the macroscopic grain size (Baxter, 2010).

Ultimately, for the samples in this study, there is a qualitative relationship between grain size of the analysed samples and the resulting age, such that the coarsest samples (such as the DoArBt4 aliquots) produce older ages than finer material (such as sample AWABv1). Additionally, an interpretation for the slight increase in age with each successive heating step shown by sample AWABv1 (Fig. 11G) is that the diffusion volume was small. As a result, some of the 'tightly bound' Ar in the crystal lattice is lost at lower temperatures than for coarser samples as the diffusion distance is much shorter in finer grains. Furthermore, as described above, sample AWABv1 from the Birimian volcaniclastic is more highly deformed than the other samples. Although individual biotite grains do not appear damaged, such deformation could have reduced the effective diffusion volume.

There are a range of other possibilities to explain variable Ar loss between different samples, including, but not limited to, post-growth geologic processes such hydrothermal alteration as well as issues during analysis such as in vacuo breakdown. Hydrothermal alteration is not thought to have had an effect on biotite grains in this study as there is no evidence that any of the chosen samples have been subjected to extensive alteration following their respective periods of biotite growth. Mineral composition has also been suggested as having a control on closure temperature with Fe-rich biotites being less retentive to Ar (Harrison et al., 1985; Grove and Harrison, 1996). This influences equation 1 above by affecting the values of E and D_0. Biotites from all lithologies at Damang exhibit a narrow range of Fe/(Fe + Mg) ratios, generally between 0.45 – 0.55 (Fig. 10). Furthermore, there is no systematic trend in composition associated with host lithology, paragenesis or measured age. Therefore, the effect of composition is not considered significant in this study.

Taking grain size to be the controlling factor on the calculated $^{40}Ar/^{39}Ar$ age, a reasonable upper estimate of diffusion volume is 500 µm, based on previous studies as discussed above (Onstott et al., 1991; Wright et al., 1991; Hess et al., 1993; Hodges et al., 1994; Markley et al., 2002; Alexandre, 2011). The smallest average grain radius that could reasonably be expected for any of these samples is approximately 100 µm, which is controlled by the smallest grain sizes. These upper and lower estimates of diffusion volume serve as initial conditions for investigating the effect of changing diffusion volume (grain size) on the measured age. A key assumption that is made here is that all grains within a sample have the same, or similar, diffusion volume. This is plausible given the relatively uniform grain sizes observed within any one sample.

Using Dodson's (1973) equation above (equation 1), for any given cooling rate, the difference in closure temperature between grains of 500 and 100 µm diameters is approximately 60ºC. The measured age range therefore represents the time taken to cool through this closure temperature interval.

5.1 DIFFARG modelling of $^{40}Ar/^{39}Ar$ results

Diffusion modelling with the program DIFFARG (Wheeler, 1996) was used to investigate the effect of grain size on $^{40}Ar/^{39}Ar$ age (Fig. 12). Details of the modelling procedure are given in Appendix 1. The best fit to measured $^{40}Ar/^{39}Ar$ ages from this study requires initial cooling at a rate of 17ºC/Ma, followed by prolonged cooling at a much slower rate of 0.15ºC/Ma for the remainder of the model run (Fig. 12A). The modelled age for a 500 µm biotite is 1978 Ma (Fig. 12E), which is within error of all aliquots for samples DoArBt4. The calculated age for a 100 µm biotite is 1919 Ma (Fig. 12F), which is within error of both samples AWDDo6 and DoArBt2 while being marginally older than sample AWABv1. This is acceptable given the uncertainty in true sample grain size. Alternatively, the younger age measured for sample AWABv1 may be a consequence of crystallographic deformation as that sample is from the Birimian volcaniclastics, which experienced regional deformation prior to deposition of the Tarkwaian System (White, 2011).

This simple two stage cooling model ultimately fits well with the measured $^{40}Ar/^{39}Ar$ ages. However, given the uncertainty on the timing of peak metamorphism (2005±26 Ma), the first stage of cooling may have commenced earlier or later than was used in the DIFFARG model. Specifically, if cooling were to have commenced earlier than 2005 Ma, then a rate as low as 7 ºC/Ma for stage 1 is required. Conversely, a later start to cooling would necessitate a higher rate of cooling up to as high as 50 ºC/Ma, which is unlikely. In contrast, cooling stage 2 is essentially fixed by the spread of measured ages and requires a much slower cooling rate. Even considering potential variation is the modelled cooling history, the general form is clear, with initial relatively rapid cooling for some 20 Ma followed by much slower cooling through the Ar closure temperature interval of biotite and below.

An important outstanding question is whether the $^{40}Ar/^{39}Ar$ ages of Pigois et al. (2003) (referred to simply as Pigois for the remainder of this section) can be incorporated into the DIFFARG model. Those ages of 2029±4 Ma and 2034±4 Ma are comparable to the upper uncertainty limit on our new U-Th-total Pb monazite age

(2005±26 Ma). Therefore, to include these data in the model requires that cooling must have commenced earlier than 2005 Ma, nearer 2030 Ma. An alternative option is also that the samples used by Pigois were coarser, or at least had a larger diffusion volume, than any samples from this study. The sample analysed by Pigois is a mineralised Tarkwa Phyllite that contains “large, separable grains”. As such, the Pigois biotites may well be coarser, and therefore provide an older age, than the samples in this study. Alternatively, they may have a significantly different composition (more Mg-rich) than samples used in this study, resulting in a higher closure temperature.

The DIFFARG model can be modified in two ways in an attempt to incorporate the Pigois data. With a lower initial cooling rate, closer to 5ºC/Ma, for example, the model still maintains a good fit to our data; as described above, the spread of measured ages is generated by the much slower second cooling stage. However, in this model, the Pigois samples would require diffusion volumes of more than 10 mm, which is both theoretically and practically unlikely, as per the discussion in the preceding section. Alternatively, if the initial cooling rate is raised significantly then the Pigois samples can be approximately fitted with more sensible diffusion volumes (approximately 1 mm) but the cooling rate must exceed 50 ºC/Ma, which is geologically unlikely.

Ultimately, given the constraints provided by the other data, the $^{40}Ar/^{39}Ar$ ages provided by Pigois et al. (2003) cannot be incorporated in to our DIFFARG model in a satisfactory way. However, it is evident that, irrespective of how the model is varied, the general form of the cooling history is consistent, with an initial cooling phase occurring at a much higher rate than a second, more prolonged cooling phase. Therefore, despite the unquantifiable uncertainty that exists on the calculated cooling rates, the model presented here is interpreted as a reasonable approach to the true thermal history at Damang.

5.2 Implications for regional tectonics and gold mineralisation

The new ages and modelled post-peak metamorphic thermal history presented here have interesting implications for regional tectonics. The short transition from relatively rapid to much slower cooling suggests a link between tectonism and exhumation in the Damang region around the time of the formation of the gold-bearing quartz vein array (event TD_3 of Tunks et al., 2004). The implied sub-vertical decompression associated with exhumation matches with the localised stress field determined for the flat-lying fault-fracture mesh at Damang, which comprises horizontal compression and vertical extension (Tunks et al., 2004). Such exhumation also provides an explanation for the young age of peak metamorphism determined here. Many staurolite and monazite-producing reactions, relevant to the Tarkwa Phyllite, possess positive P/T slopes, such that they may be crossed during decompression (Spear, 2010). Therefore, the U-Th-total Pb age of 2005±26 Ma is interpreted as a minimum age for the commencement of exhumation and not the time that maximum P-T conditions were initially reached. The extent of this exhumation would appear to be spatially restricted. Tarkwa mine, situated approximately 30 km SW of Damang (Fig. 1A), contains paleoplacer-style mineralisation hosted by Tarkwaian System sediments similar to those at Damang. However, metamorphic mineral assemblages at Tarkwa do not exceed greenschist facies. This, coupled with the lack of a Damang-style fault-fracture mesh suggests that Tarkwa has not undergone the same degree of metamorphism and subsequent exhumation. The faults required to drive exhumation, however, are not visible within the Damang camp (Fig. 1B) and are inferred to be located outboard of the Damang anticline.

Although the ages for peak metamorphism (2005±26 Ma) and cooling (1980±9 Ma to 1898±11 Ma) presented here are significantly younger than previous estimates from elsewhere in Ghana, occurring in the very late stages of the Eburnean orogeny, they provide an internal consistency that broadly correlates with the regional framework. Specifically, they fit well with the regional geodynamic model of Perrouty et al. (2012) with only a modification to the timing of their D6 event (event TD_3 of Tunks et al. (2004)) that represents hydrothermal gold mineralisation at Damang. Perrouty et al. (2012) placed this event at 2063±9 Ma, based on the U/Pb xenotime age of Pigois et al. (2003). We propose that in fact this event is at least 30 Ma younger, falling between approximately 2030 Ma and 1980 Ma, constrained between our new ages for metamorphism and cooling.

6. Conclusions

In this paper we present new geochronological data constraining the timing of volcanic activity, regional metamorphism and cooling at the Damang gold deposit. Birimian volcanism occurred at 2178.0±9.3 Ma, which is consistent with ages available from elsewhere in Ghana (Fig. 13). Birimian volcanic rocks were intruded by the Diorite Porphyry at 2164.6±8.0 Ma, all prior to deposition of the Tarkwaian System sediments. Monazite-producing reactions associated with staurolite-grade, amphibolites facies metamorphism, occurred at 2005±26 Ma. This time marks the minimum age for the onset of localised exhumation that initiated cooling of the Damang region at a rate of approximately 17ºC/Ma and persisted for around 20 Ma. This cooling rate is poorly constrained, primarily due to the uncertainty associated with the age of metamorphism, and can vary within plus or minus a factor of about two to three. The initial phase of cooling was followed by a prolonged period of slow cooling at a rate of approximately 0.15ºC/Ma, as constrained by a range of $^{40}Ar/^{39}Ar$ biotite ages between 1980±9 Ma and 1898±11 Ma. Hydrothermal gold mineralisation at Damang is inferred to have occurred between approximately 2030 Ma and 1980 Ma. These ages for metamorphism and cooling are younger than any previously reported for SW Ghana and represent the latest stage of the Eburnean orogeny currently recognised (Fig. 13). Furthermore, these data suggest that orogenic gold mineralisation is significantly younger at the Damang deposit than orogenic gold deposits elsewhere in Ghana and this is reflected in Damang's differing tectonic history. Consequently, the Damang event represents a distinct and discrete phase of gold deposition in West Africa's prolonged metallogenic evolution.

More importantly, although Damang is unique amongst currently known Ghanaian gold deposits, its tectonic history is not necessarily so. Therefore, it is plausible that other locally exhumed regions of the Birimian terrane, particularly in the Tarkwaian System, are prospective for Damang-style gold mineralisation. Ultimately, hydrothermal gold mineralisation in the Tarkwaian System may represent a significantly underexplored resource.

Acknowledgements

The authors gratefully acknowledge the thorough and helpful reviews of David Phillips and Randall Parrish, whose comments significantly improved this manuscript.. Gold Fields Ltd. funded this work through the Ph.D. sponsorship of A. White. In this regard, Ed Baltis is thanked for his support. The exploration team at Damang mine, in particular Jason Kavanagh and Deon Steenkamp, are thanked for fieldwork support. Kerstin Lindén and Will Brownscombe are thanked for their assistance with zircon separation in Stockholm. Steve Wyatt is thanked for his assistance with sulphide and biotite separation. Clare Warren is gratefully acknowledged for her advice regarding DIFFARG modelling. The useful comments of Adam Bath and Iris Sonntag greatly improved an earlier version of this manuscript.

References

Abouchami, W., Boher, M., Michard, A., Albarede, F., 1990. A major 2.1 Ga event of mafic magmatism in West Africa: an early stage of crustal accretion. Journal of Geophysical Research 95, 17605-17629.

Alexandre, P., 2011. Comparison between grain size and multi-mineral $^{40}Ar/^{39}Ar$ thermochronology. Geochimica et Cosmochimica Acta 75, 4260-4272.

Allibone, A., Teasdale, J., Cameron, G., Etheridge, M., 2002. Timing and structural controls on gold mineralization at the Bogoso gold mine, Ghana, West Africa. Economic Geology 97, 949-969.

Ancey, M., Bastenaire, F., Tixier, R., 1978. Application des méthodes statistiques en microanalyse, in: Microanalyse, Microscopie Électronique à Balayage. Les Éditions du Physicien, Orsay, p. 323-347.

Barra, F., Ruiz, J., Mathur, R., Titley, S., 2003. A Re-Os study of sulfide minerals from the Bagdad porphyry Cu-Mo deposit, northern Arizona, USA. Mineralium Deposita 38, 585-596.

Baxter, E.F., 2010. Diffusion of noble gases, in: Zhang, Y., Cherniak, D.J. (Eds), Diffusion in Minerals and Melts. Reviews in Mineralogy and Geochemistry 72.

Berge, J., 2011. Paleoproterozoic, turbidite-hosted, gold deposits of the Ashanti gold belt (Ghana, West Africa): Comparative analysis of turbidite-hosted gold deposits and an updated genetic model. Ore Geology Reviews 1-10.

Boher, M., Abouchami, W., Michard, A., Albarede, F., Arndt, N., 1992. Crustal growth in West Africa at 2.1 Ga. Journal of Geophysical Research 97, 345-369.

Brenan, J., Cherniak, D., Rose, L., 2000. Diffusion of osmium in pyrrhotite and pyrite: implications for closure of the Re-Os isotopic system. Earth and Planetary Science Letters 180, 399-413.

Brownscombe, W., 2009. The Tinga anomaly: A new style of gold mineralization in Ghana? MESc thesis, University of Oxford.

Buick, I.S., Maas, R., Gibson, R., 2001. Precise U-Pb titanite age constraints on the emplacement of the Bushveld Complex, South Africa. Journal of the Geological Society, London 158, 3-6.

Cardon, O., Reisberg, L., Andre-Mayer, A., Leroy, J., Milu, V., Zimmermann, C., 2008. Re-Os systematics of pyrite from the Bolcana porphyry copper deposit, Apuseni Mountains, Romania. Economic Geology 103, 1695-1702.

Catlos, E., Harrison, T., Kohn, M., Grove, M., Ryerson, F., Manning, C., Upreti, B., 2001. Geochronologic and thermobarometric constraints on the evolution of the Main

Central Thrust, central Nepal Himalaya. Journal of Geophysical Research 106, 16177-16204.

Cocherie, A., Legendre, O., Peucat, J., Kouamelan, A., 1998. Geochronology of polygenetic monazites constrained by in situ electron microprobe Th-U-total lead determination: Implications for lead behaviour in monazite. Geochimica et Cosmochimica Acta 62, 2475-2497.

Corrie, S., Kohn, J., 2008. Trace-element distributions in silicates during prograde metamorphic reactions: implications for monazite formation. Journal of Metamorphic Geology 26, 451-464.

Dampare, S., Shibata, T., Asiedu, D., Osae, S., Banoeng-Yakubo, B., 2008. Geochemistry of Paleoproterozoic metavolcanic rocks from the southern Ashanti volcanic belt, Ghana: Petrogenetic and tectonic setting implications. Precambrian Research 162, 403-423.

Davis, D., Hirdes, W., Schaltegger, U., Nunoo, E., 1994. U-Pb age constraints on deposition and provenance of Birimian and gold-bearing Tarkwaian sediments in Ghana, West Africa. Precambrian Research 67, 89-107.

Dini, A., Rocchi, S., Westerman, D., 2004. Reaction microtextures of REE-Y-Th-U accessory minerals in the Monte Capanne pluton (Elba Island, Italy): a possible indicator of hybridization processes. LITHOS 78, 101-118.

Dodson, M., 1973. Closure temperature in cooling geochronological and petrological systems. Contributions to Mineralogy and Petrology 40, 259-274.

Eisenlohr, B., 1992. Conflicting evidence on the timing of mesothermal and paleoplacer gold mineralisation in early Proterozoic rocks from southwest Ghana, West Africa. Mineralium Deposita 27, 23-29.

Eisenlohr, B.N., Hirdes, W., 1992. The structural development of the early Proterozoic Birimian and Tarkwaian rocks of southwest Ghana, West Africa. Journal of African Earth Sciences 14, 313-325.

Ennih, N., Liégeois, J., 2008. The boundaries of the West African craton, with special reference to the basement of the Moroccan metacratonic Anti-Atlas belt. Geological Society London Special Publications 297, 1-17.

Feybesse, J., Billa, M., Guerrot, C., Duguey, E., Lescuyer, J., Milési, J., Bouchot, V., 2006. The paleoproterozoic Ghanaian province: Geodynamic model and ore controls, including regional stress modeling. Precambrian Research 149, 149-196.

Feybesse, J.L., Milési, J.P., 1994. The Archean/Proterozoic contact zone in West Africa: a mountain belt of décollement thrusting and folding on a continental margin related to 2.1 Ga convergence of Archean cratons? Precambrian Research 69, 199-227.

Finger, F., Broska, I., Roberts, M., Schermaier, A., 1998. Replacement of primary monazite by apatite-allanite-epidote coronas in an amphibolite facies granite gneiss from the eastern Alps. American Mineralogist 83, 248-258.

Goldfarb, R., Baker, T., Dubé, B., Groves, D., Hart, C., Gosselin, P., 2005. Distribution, character, and genesis of gold deposits in metamorphic terranes. Economic Geology 100th Anniversary Volume, 407-450.

Goldfarb, R., Groves, D., Gardoll, S., 2001. Orogenic gold and geologic time: a global synthesis. Ore Geology Reviews 18, 1-75.

Grove, M., Harrison, T.M., 1996. $^{40}Ar^*$ diffusion in Fe-rich biotite. American Mineralogist 81, 940-951.

Harcouët, V., Guillou-Frottier, L., Bonneville, A., Bouchot, V., Milési, J., 2007. Geological and thermal conditions before the major Palaeoproterozoic gold-mineralization event at Ashanti, Ghana, as inferred from improved thermal modelling. Precambrian Research 154, 71-87.

Harmer, R.E., Armstrong, R.A., 2000. Duration of Bushveld Complex (sensu lato) magmatism: constraints from new SHRMIP zircon chronology. Abstracts, Bushveld Complex Workshop, National research Foundation, Gethlane Lodge, South Africa. American Geophysical Union.

Harrison, T.M., Duncan, I., McDougall, I., 1985. Diffusion of ^{40}Ar in biotite: temperature, pressure and compositional effects. Geochimica et Cosmochimica Acta 49, 2461-2468.

Hein, K., 2010. Succession of structural events in the Goren greenstone belt (Burkina Faso): Implications for West African tectonics. Journal of African Earth Sciences 56, 83-94.

Hess, J., Lippolt, H., Gurbanov, A., Michalski, I., 1993. The cooling history of the late Pliocene Eldzhurtinskiy granite (Caucasus, Russia) and the thermochronological potential of grain-size/age relationships. Earth and Planetary Science Letters 117, 393-406.

Hirdes, W., Davis, D., 1998. First U-Pb zircon age of extrusive volcanism in the Birimian Supergroup of Ghana/West Africa. Journal of African Earth Sciences 27, 291-294.

Hirdes, W., Davis, D., 2002. U-Pb Geochronology of Paleoproterozoic Rocks in the Southern Part of the Kedougou-Kéniéba Inlier, Senegal, West Africa: evidence for diachronous accretionary development of the Eburnean Province. Precambrian Research 118, 83-99.

Hirdes, W., Davis, D., Eisenlohr, B., 1992. Reassessment of Proterozoic granitoid ages in Ghana on the basis of U/Pb zircon and monazite dating. Precambrian Research 56, 89-96.

Hodges, K., Harries, W., Bowring, S., 1994. 40Ar/39Ar age gradients in micas from a high-temperature-low-pressure metamorphic terrain: Evidence for very slow cooling and implications for the interpretation of age spectra. Geology 22, 55-58.

Janots, E., Engi, M., Berger, A., Allaz, J., Schwarz, J.-O., Spandler, C., 2008. Prograde metamorphic sequence of REE minerals in pelitic rocks of the Central Alps: implications for allanite-monazite-xenotime phase relations from 250 to 610ºC. Journal of Metamorphic Geology 26, 509-526.

John, T., Klemd, R., Hirdes, W., Loh, G., 1999. The metamorphic evolution of the Paleoproterozoic (Birimian) volcanic Ashanti belt (Ghana, West Africa). Precambrian Research 98, 11-30.

Jourdan, F., Verati, C., Féraud, G., 2006. Intercalibration of the Hb3gr $^{40}Ar/^{39}Ar$ dating standard. Chemical Geology 231, 77-189.

Klemd, R., Hunken, U., Olesch, M., 2002. Metamorphism of the country rocks hosting gold-sulfide bearing quartz-veins in the Paleoproterozoic southern Kibi-Winneba belt (SE-Ghana). Journal of African Earth Sciences 35, 199-211.

de Kock, G., Armstrong, R.A., Siegfried, H.P., Thomas, E., 2011. Geochronology of the Birim Supergroup of the West African craton in the Wa-Bolé region of west-central Ghana: Implications for the stratigraphic framework. Journal of African Earth Sciences 59, 1-40

Kohn, M., Malloy, M., 2004. Formation of monazite via prograde metamorphic reactions among common silicates: Implications for age determination. Geochimica et Cosmochimica Acta 68, 101-113.

Ledru, P., Johan, V., Milési, J.P., Tegyey, M., 1994. Markers of the last stages of the Palaeoproterozoic collision: evidence for a 2 Ga continent involving circum-South Atlantic provinces. Precambrian Research 69, 169-191.

Lee, J., 1995. Multipath diffusion in geochronology. Contributions to Mineralogy and Petrology 120, 60-82.

Leube, A., Hirdes, W., Mauer, R., Kesse, G., 1990. The early Proterozoic Birimian Supergroup of Ghana and some aspects of its associated gold mineralization. Precambrian Research 46, 139-165.

Lisowiec, N., 2006. Precision estimation in electron microprobe monazite dating: Repeated measurements versus statistical (Poisson) based calculations. Chemical Geology 234, 223-235.

Loh, G., Hirdes, W., Anani, C., Davis, D.W., Vetter, U., 1999. Explanatory notes for the geological map of Southwest Ghana 1:1000,000. Geologisches Jahrbuch B 93, 150.

Ludwig, K., 2003. User's Manual for Isoplot 3.00. A geochronological toolkit for Microsoft Excel, Berkeley Geochronology Center Special Publication. Berkeley Geochronology Center Special Publication, 1-71.

Ludwig, K.R., 1980. Calculation of uncertainties of U-Pb isotope data. Earth and Planetary Science Letters 46, 212-220.

Markley, M., Teyssier, C., Cosca, M., 2002. The relation between grain size and $^{40}Ar/^{39}Ar$ date for Alpine white mica from the Siviez-Mischabel Nappe, Switzerland. Journal of Structural Geology 24, 1937-1955.

McDougall, I., Harrison, T.M., 1999. Geochronology and thermochronology by the $^{40}Ar/^{39}Ar$ method, 2nd ed. Oxford University Press, Oxford.

Milési, J., Ledru, P., Feybesse, J., Dommanget, A., Marcoux, E., 1992. Early proterozoic ore deposits and tectonics of the Birimian orogenic belt, West Africa. Precambrian Research 58, 305-344.

Milési, J., Ledru, P., Ankrah, P., Johan, V., Marcoux, E., 1991. The metallogenic relationship between Birimian and Tarkwaian gold deposits in Ghana. Mineralium Deposita 26, 228-238.

Montel, J., Foret, S., Veschambre, M., Nicollet, C., Provost, A., 1996. Electron microprobe dating of monazite. Chemical Geology 131, 37-53.

Morelli, J.M., 2008. Rhenium-osmium geochronology of low-level sulfide minerals from hydrothermal ore deposits - Applications, limitations, and implications. PhD thesis, University of Alberta.

Mumin, A., Fleet, M., 1995. Evolution of gold mineralization in the Ashanti Gold Belt, Ghana: Evidence from carbonate compositions and parageneses. Mineralogy and Petrology 55, 265-280.

Mumin, A.H., Fleet, M.E., Longstaff, F.J., 1996. Evolution of hydrothermal fluids in the Ashanti Gold Belt, Ghana: Stable isotope geochemistry of carbonates, graphite, and quartz. Economic Geology 91, 135-148.

Oberthür, T., Vetter, U., Davis, D., Amanor, J., 1998. Age constraints on gold mineralization and Paleoproterozoic crustal evolution in the Ashanti belt of southern Ghana. Precambrian Research 89, 129-143.

Oberthür, T., Weiser, T., Amanor, J., Chryssoulis, S., 1997. Mineralogical siting and distribution of gold in quartz veins and sulfide ores of the Ashanti mine and other deposits in the Ashanti belt of Ghana: genetic implications. Mineralium Deposita 32, 2-15.

Onstott, T., Phillips, D., Pringle-Goodell, L., 1991. Laser microprobe measurement of chlorine and argon zonation in biotite. Chemical Geology 90, 145-168.

Parrish, R., 1990. U-Pb dating of monazite and its application to geological problems. Canadian Journal of Earth Sciences 27, 1431-1450.

Perrouty, S., Aillères, L., Jessell, M.W., Baratoux, L., Bourassa, Y., Crawford, B., 2012. Revised Eburnean geodynamic evolution of the gold-rich southern Ashanti Belt, Ghana, with new field and geophysical evidence of pre-Tarkwaian deformations. Precambrian Research 204-205, 12-39.

Phillips, D., Onstott, T.C., 1988. Argon isotopic zoning in mantle phlogopite. Geology 16, 542-546.

Pigois, J.P., Groves, D.I., Fletcher, I.R., McNaughton, N.J., Snee, L.W., 2003. Age constraints on Tarkwaian palaeoplacer and lode-gold formation in the Tarkwa-Damang district, SW Ghana. Mineralium Deposita 38, 695-714.

Rasmussen, B., Muhling, J.R., 2009. Reactions destroying detrital monazite in greenschist-facies sandstones from the Witwatersrand basin, South Africa. Chemical Geology 264, 311-327.

Scherrer, N., Engi, M., Gnos, E., Jakob, V., Liechti, A., 2000. Monazite analysis; from sample preparation to microprobe age dating and REE quantification. Schweizerische Mineralogische und Petrographische Mittellungen 80, 93-105.

Schmidt Mumm, A., Oberthür, T., Vetter, U., Blenkinsop, T., 1997. High CO_2 content of fluid inclusions in gold mineralisations in the Ashanti Belt, Ghana: a new category of ore forming fluids? Mineralium Deposita 32, 107-118.

Scoates, J.S., Friedman, R.M., 2008. Precise age of the platiniferous Merensky Reef, Bushveld Complex, South Africa, by the U-Pb zircon chemical abrasion ID-TIMS technique. Economic Geology 103, 465-471.

Selby, D., Creaser, R., Stein, H., Markey, R., Hannah, J., 2007. Assessment of the ^{187}Re decay constant by cross calibration of Re-Os molybdenite and U-Pb zircon chronometers in magmatic ore systems. Geochimica et Cosmochimica Acta 71, 1999-2013.

Selby, D., Kelley, K., Hitzman, M., Zieg, J., 2009. Re-Os Sulfide (Bornite, Chalcopyrite and Pyrite) Systematics of the Carbonate-Hosted Copper Deposits at Ruby Creek, Southern Brooks Range, Alaska. Economic Geology 104, 437-444.

Smoliar, M.I., Walker, R.J., Morgan, J.W., 1996. Re-Os ages of group IIa, IIIA, IVA, and IVB iron meteorites. Science 271, 1099-1102.

Spear, F.S., 2010. Monazite-allanite phase relations in metapelites. Chemical Geology 279, 55-62.

Spear, F.S., Pyle, J.M., Cherniak, D., 2009. Limitations of chemical dating of monazite. Chemical Geology 266, 218-230.

Steiger, R.H., Jäger, E., 1977. Subcommision on geochronology - Convention on the use of decay constants in geo- and cosmochronology. Earth and Planetary Science Letters 36, 359-362.

Suzuki, K., Adachi, M., 1991. Precambrian provenance and Silurian metamorphism of the Tsubonosawa paragneiss in the South Kitakami terrane, Northeast Japan, revealed by the chemical Th-U-total Pb isochron ages of monazite, zircon and xenotime. Chemical Geology 25, 357-376.

Suzuki, K., Adachi, M., Kajizuka, I., 1994. Electron microprobe observations of Pb diffusion in metamorphosed detrital monazites. Earth and Planetary Science Letters 128, 391-405.

Suzuki, K., Adachi, M., Tanaka, T., 1991. Middle Precambrian provenance of Jurassic sandstone in the Mino Terrane, central Japan: Th-U-total Pb evidence from an electron microprobe monazite study. Sedimentary Geology 75, 141-147.

Taylor, P., Moorbath, S., Leube, A., Hirdes, W., 1992. Early Proterozoic crustal evolution in the Birimian of Ghana: constraints from geochronology and isotope geochemistry. Precambrian Research 56, 97-111.

Tomkins, H., Pattison, D., 2007. Accessory phase petrogenesis in relation to major phase assemblages in pelites from the Nelson contact aureole, southern British Columbia. Journal of Metamorphic Geology 25, 401-421.

Townsend, K., Miller, C., D'Andrea, J., Ayers, J., Harrison, T., Coath, C., 2000. Low temperature replacement of monazite in the Ireteba granite, Southern Nevada: geochronological implications. Chemical Geology 172, 95-112.

Tunks, A., Selley, D., Rogers, J., Brabham, G., 2004. Vein mineralization at the Damang Gold Mine, Ghana: controls on mineralization. Journal of Structural Geology 26, 1257-1273.

Upadhyay, D., Pruseth, K.L., 2012. Fluid-induced dissolution breakdown of monazite from Tso Morari complex, NW Himalayas: evidence for immobility of trace elements. Contributions to Mineralogy and Petrology 164, 303-316.

Wheeler, J., 1996. DIFFARG: a program for simulating argon diffusion profiles in minerals. Computers & Geosciences 22, 919-929.

White, A.J.R., Robb, V.M., Robb, L.J., Waters, D.J., 2010. Portable infrared spectroscopy as a tool for the exploration of gold deposits in tropical terrains: A case study at the Damang deposit, Ghana. Society of Economic Geologists Special Publication 15, 67-84.

White, A.J.R., Waters, D.J., Robb, L.J., 2013. The application of P-T-X(CO_2) modelling in constraining metamorphism and hydrothermal alteration at the Damang gold deposit, Ghana, Journal of Metamorphic Geology, 31, 937-961.

Whitehouse, M.J., Claesson, S., Sunde, T., Vestin, J., 1997. Ion microprobe U-Pb zircon geochronology and correlation of Archaean gneisses from the Lewisian Complex of Gruinard Bay, northwestern Scotland. Geochimica et Cosmochimica Acta 61, 4429-4438.

Whitehouse, M.J., Kamber, B., 2005. Assigning Dates to Thin Gneissic Veins in High-Grade Metamorphic Terranes: A Cautionary Tale from Akilia, Southwest Greenland. Journal of Petrology 46, 291-318.

Whitehouse, M.J., Kamber, B., Moorbath, S., 1999. Age significance of U-Th-Pb zircon data from early Archaean rocks of west Greenland - a reassessment based on combined ion-microprobe and imaging studies. Chemical Geology 160, 201-224.

Wiedenbeck, M., Allé, P., Corfu, F., Griffin, W., Meier, M., Oberli, F., Quadt, A.V., Roddick, J., Spiegel, W., 1995. Three natural zircon standards for U-Th-Pb, Lu-Hf, trace element and REE analysis. Geostandards Newsletter 19, 1-23.

Wille, S.E., Klemd, R., 2004. Fluid inclusion studies of the Abawso gold prospect, near the Ashanti Belt, Ghana. Mineralium Deposita 39, 31-45.

Williams, M., Jercinovic, M., 2002. Microprobe monazite geochronology: putting absolute time into microstructural analysis. Journal of Structural Geology 24, 1013-1028..

Wing, B., Ferry, J., Harrison, T., 2003. Prograde destruction and formation of monazite and allanite during contact and regional metamorphism of pelites: petrology and geochronology. Contributions to Mineralogy and Petrology 145, 228-250.

Wright, N., Layer, P., York, D., 1991. New insights into thermal history from single grain $^{40}Ar/^{39}Ar$ analysis of biotite. Earth and Planetary Science Letters 104, 70-79.

Yao, Y., Murphy, P., Robb, L., 2001. Fluid characteristics of granitoid-hosted gold deposits in the Birimian Terrane of Ghana: a fluid inclusion microthermometric and Raman spectroscopic study. Economic Geology 96, 1611-1643.

Appendix 1

Analytical and modelling techniques

U/Pb analysis of zircon

Analysis of separated zircons was undertaken using the NORDSIM Cameca IMS 1280 large- format ion microprobe secondary ionization mass spectrometer (SIMS) at the Naturhistoriska Riksmuseet in Stockholm, Sweden. Analytical procedures were similar to those described by Whitehouse et al. (1997; 1999) and Whitehouse and Kamber (2005) and briefly summarized here. A c. 8 nA defocused O_2^- primary beam was used to project the image of a 150 μm aperture onto the sample, producing an elliptical, flat-bottomed crater with an approximately 20 μm long axis. An energy window of 60 eV was used in the secondary ion beam optics with energy adjustments made using the $^{90}Zr^{16}O$ peak. U-Pb analyses with a mass resolution (M/ΔM) of c. 5000 were performed using a peak switching routine, with a single ion-counting electron multiplier as the detection device. Mass calibration was maintained using the automatic routine in the Cameca CIPS software. Pb/U calibration was performed relative to Geostandards zircon 91500 with an accepted age of 1065.4±0.3 Ma (1σ) and Pb and U concentrations of c. 15 and 80 ppm respectively (Wiedenbeck et al., 1995). Data reduction was performed using Isoplot/Ex v.3.7 (Ludwig, 2003).

U-Th-Total Pb analysis of monazite

Chemical analyses of monazite grains were carried out in situ in thin section. Prior to this, monazite grains were identified using a scanning electron microscope at the University of Oxford, based on their high backscatter coefficient and EDS spectrum. Grains were also assessed for compositional zonation, particularly with regards to Th content. A total of 53 monazites were analysed, from two unmineralised (AWDP1 and AWDBm1) and one mineralised (AWDP2) sample. Quantitative analysis of identified monazite grains was completed at the University of Oxford using a JEOL JXA-8800R EPMA operating at 15 kV and 60 nA to allow for optimal spatial resolution of approximately 0.5 µm with an estimated excitation volume of approximately 2 µm. The EPMA is equipped with four wavelength-dispersive spectrometers. An internal age standard, sample DLB-22A, was used to standardise the age distribution. DLB-22A is a garnet-cordierite pelitic hornfels from the inner aureole of the eastern Bushveld complex near the Steelpoort pericline and contains numerous large monazites. Since the monazite grew during thermal metamorphism resulting from the intrusion of the Bushveld complex, the intrusion age of 2057.5±4.2 Ma at this location

(Harmer and Armstrong, 2000) is comparable to other estimates of the Bushveld intrusion age (2058.9±0.8 Ma (Buick et al., 2001) and 2054.4±1.3 Ma (Scoates and Friedmand, 2008)) and is a reliable measure of the timing of monazite growth. Concentration errors and detection limits were calculated using the Poisson (counting) statistics approach of Ancey et al. (1978) with individual age errors calculated according to Montel et al. (1996). The final age and associated uncertainty was obtained using population statistics (Williams and Jercinovic, 2002). Errors associated with the final age are given at a 95% confidence interval, as recommended by Lisowiec (2006).

Compositional analysis of biotite

Biotite mineral compositions were determined using a JEOL JSM-840A scanning electron microscope, fitted with an Oxford Instruments Isis 300 energy-dispersive analytical spectrometer, located in the Department of Earth Sciences, University of Oxford. Standard analytical conditions comprised a 20 kV accelerating voltage, 5 nA beam current that was monitored regularly, and a live beam counting time of 100 s. Elemental calibrations were made against a range of natural and synthetic standards, a ZAF correction procedure was used and the count rate was calibrated approximately every 1 – 2 h using a pure cobalt metal standard.

$^{40}Ar/^{39}Ar$ analysis of biotite

Biotite separates were prepared by lightly crushing bulk rocks, followed by hand-picking grains under a binocular microscope. The biotite samples were washed in deionised water and acetone and dried under an infrared heating lamp. Between 0.009-0.0012 grams of samples were weighed and wrapped in aluminium foil before being loaded into quartz vials for irradiation. Hb3gr age monitors (t = 1073.6±5.3 Ma; Jourdan et al., 2006) were regularly spaced between samples to monitor neutron fluence variations, and pure K_2SO_4 and CaF_2 were included to determine the neutron interference reactions for Ar isotopes. The quartz vials were sealed and irradiated at RODEO I4 position of the High Flux Reactor, Petten, the Netherlands, with a fast neutron fluence of approximately 2×10^{18} n/cm^2, as determined from the Hb3gr monitors. Samples were step heated in a Ta-resistance furnace over the temperature interval 400-1400°C using 30 minute steps. Noble gases released during each step were purified using a Zr-Al getter at 400°C. At the end of each temperature step the gases were transferred to the inlet of the mass spectrometer by freezing in liquid nitrogen on activated charcoal. Argon gas was released from the charcoal by heating to 80°C, and then admitted to the mass spectrometer for isotopic analysis. The MS1 mass spectrometer is a single focussing 90° sector instrument equipped with a Faraday detector. Ions are produced using a Baur-Signer ion source with a sensitivity of 4.4×10^{-4} amps/torr. Isotopic determinations of argon isotopes (m/z 36, 37, 38 39 and 40) and baseline readings (at half masses) are carried out over 11 cycles by peak switching the magnetic field. Following acquisition, the data are regressed to obtain a consistent set of readings at the gas inlet time. The data are further reduced by applying corrections for mass discrimination obtained from aliquots of atmospheric argon, and neutron interference reactions. Minor corrections were applied for neutron interference reactions using the following values: $(^{40}Ar/^{39}Ar)_K = 0.0126$; $(^{38}Ar/^{39}Ar)_K = 0.012$; $(^{39}Ar/^{37}Ar)_{Ca} = 0.000267$; $(^{36}Ar/^{37}Ar)_{Ca} = 0.000666$. $(^{40}Ar/^{39}Ar)$K was determined from the K_2SO_4 monitor. Argon blank corrections were not applied to the data because the levels represented <1% of a typical Ar release and are isotopically indistinguishable from atmospheric argon. $^{40}Ar/^{39}Ar$ ages were determined from age spectrum diagrams, using the Isoplot/Ex v.3.7 software (Ludwig, 2003) and the decay constant of Steiger and Jäger (1977). An age plateau was defined by at least 60% of released ^{39}Ar in three or more continguous steps. The calculated final age was determined by summing the AR released over the defined plateau interval. Unless otherwise stated, all data are reported at the 1σ level of uncertainty. Final ages are given at 2σ uncertainty and exclude uncertainties on the J value.

DIFFARG modelling methods

Numerical modelling of Ar diffusion in biotites was undertaken with the program DIFFARG (Wheeler, 1996). The diffusion parameters of Grove and Harrison (1996) and the Crank-Nicholson algorithm, with a time step of 10, were used for the calculations. Models were run with 20, 40 and 80 radial mesh nodes and then regressed against resulting bulk sample age to give the best estimate for modelled sample age at infinite mesh nodes, i.e. a continuous diffusion profile. Cooling histories were varied in order to match model and measured ages. All models were run with no Ar atmosphere in the pore fluid and a fixed grain rim apparent age of 0 Ma. This is a first-order assumption as there is no evidence on which to base an Ar atmosphere. Furthermore, there is no recognisable metamorphic pre-history and the first significant prograde metamorphism (as is the case at Damang) should not be expected to have a significant Ar atmosphere. Models were run for a total of 400 Ma to ensure that a fully closed system was reached.

Figure Captions

Fig. 1. Simplified geology of SW Ghana (A) showing the locations of major gold deposits, including the Damang deposit (modified from Pigois et al. (2003)). Simplified geologic map (B) and stratigraphic column (C) of the Damang region (modified from Tunks et al., 2004). Fold and thrust terminology from Tunks et al. (2004).

Fig. 2. Photograph of gold-bearing extensional quartz veins in the east wall of the Damang pit. Veins are predominantly sub-horizontal with a high aspect ratio and cross-cut all earlier structures. After White et al. (2010).

Fig. 3. Photographs and photomicrographs of the Diorite Porphyry (A-C) and Birimian volcaniclastic rock (D-F).

Fig. 4. Backscattered electron images of representative monazite grains in the Tarkwa Phyllite. Unaltered grains in samples AWDP1 (A-D) occur in the matrix amongst quartz, plagioclase and muscovite (A, B) and are homogeneous (C, D) with no discernible compositional variation. Monazite in altered sample AWDP2 (E, F) are reacted to a relic grain surrounded by zones of apatite (Ap), allanite (Aln) and epidote (Ep).

Fig. 5. Photographs and photomicrographs of biotite flakes in unaltered and mineralised rocks at Damang. Coarse biotite flakes within a quartz vein, sample

DoArBt4 (A), and hydrothermal biotite in a mineralised dolerite, sample AWDDo6 (B). Additional biotite flakes can be seen in Figure 3.

Fig. 6. Representative cathodoluminescence (left) and optical (right) images of zircon crystals from the Birimian volcaniclastic, sample AWABv (A), and Diorite porphyry, sample AWADi (B). The analysis spot is approximately one quarter of the size and located in the centre of the sputtering spot visible on the optical images. Diorite Porphyry zircons are unzoned, while those in the Birimian volcaniclastic are strongly zoned, often with distinct core and rim domains.

Fig. 7. U/Pb Concordia plots for the Birimian volcaniclastic (sample AWABv) (A) and Diorite Porphyry (sample AWADi) (B).

Fig. 8. Plots of compositional variation (A-D) and REE patterns (E) for monazite grains in the Tarkwa Phyllite. All samples are tightly clustered and indistinguishable. Y is plotted in place of Ho where concentrations are below detection limits.

Fig. 9. Results of U-Th-total Pb chemical dating of all monazite grains from the Tarkwa Phyllite. Data are presented as a histogram similar to Montel et al. (1996) (A), where the small bell-curves are the probability functions for each analysed grain and the thick line of the sum of all of these functions. Data are also presented according to the isochron method of Suzuki and Adachi (1991) (B) and as a weighted average plot (C).

Fig. 10. Compositional plot of X(Mg) (Mg/(Fe+Mg)) versus octahedral Al content (cations per formula unit based on 22 oxygens) in biotites from lithologies used for $^{40}Ar/^{39}Ar$ analysis. Compositions for $^{40}Ar/^{39}Ar$ samples TpArBtt1, DoArBt2 and AWDDo6 are represented by petrographic samples AWDP1, AWDDo1 and AWDDo4 respectively, which are separate pieces of rock, but were collected from the same location and/or drill core depth.

Fig. 11. $^{40}Ar/^{39}Ar$ step-heating plateaux for all samples. All plateaux are well defined. Each sample is shown with its final age, uncertainty, number of heating steps that define the plateau and the percentage of released ^{39}Ar that comprises the plateau.

Fig. 12. Results of DIFFARG modelling of measured $^{40}Ar/^{39}Ar$ ages. A) The modelled cooling history. B) Apparent sample age, as calculated in the model, versus model run time showing how smaller grains produce younger ages than coarser grains. The main figure shows the first 50 Ma of the model run, while the inset shows the full 400 Ma of the run. C and D) Apparent age as a function of position in 500μm (C) and 100 μm (D) biotite grains, with profiles drawn every 10 Ma for the first 50 Ma of the model. E and F) Plots of apparent bulk age as a function of model mesh size for a 500μm (E) and 100μm (F) biotite grain. Final model age is given by the y-axis intercept of a regression line through these data points.

Fig. 13. A summary diagram of existing and new geochronological data for southwest Ghana. New age constraints for staurolite-grade regional metamorphism and post-metamorphic cooling at Damang are notably younger than existing data elsewhere in Ghana. See section 2.1 for sources of existing data.

Table Captions

Table 1. Summary of samples used for each analytical technique, giving the analysed mineral, the host lithology and paragenesis.

Table 2. SIMS U/Pb analytical data.

Table 3. EPMA U-Th-total Pb analytical data.

Table 4. Averaged biotite analyses from lithologies used $^{40}Ar/^{39}Ar$ analysis.

Table 5. ^{40}Ar-^{39}Ar analytical data. 2σ errors unless otherwise stated. nd = not determinable.

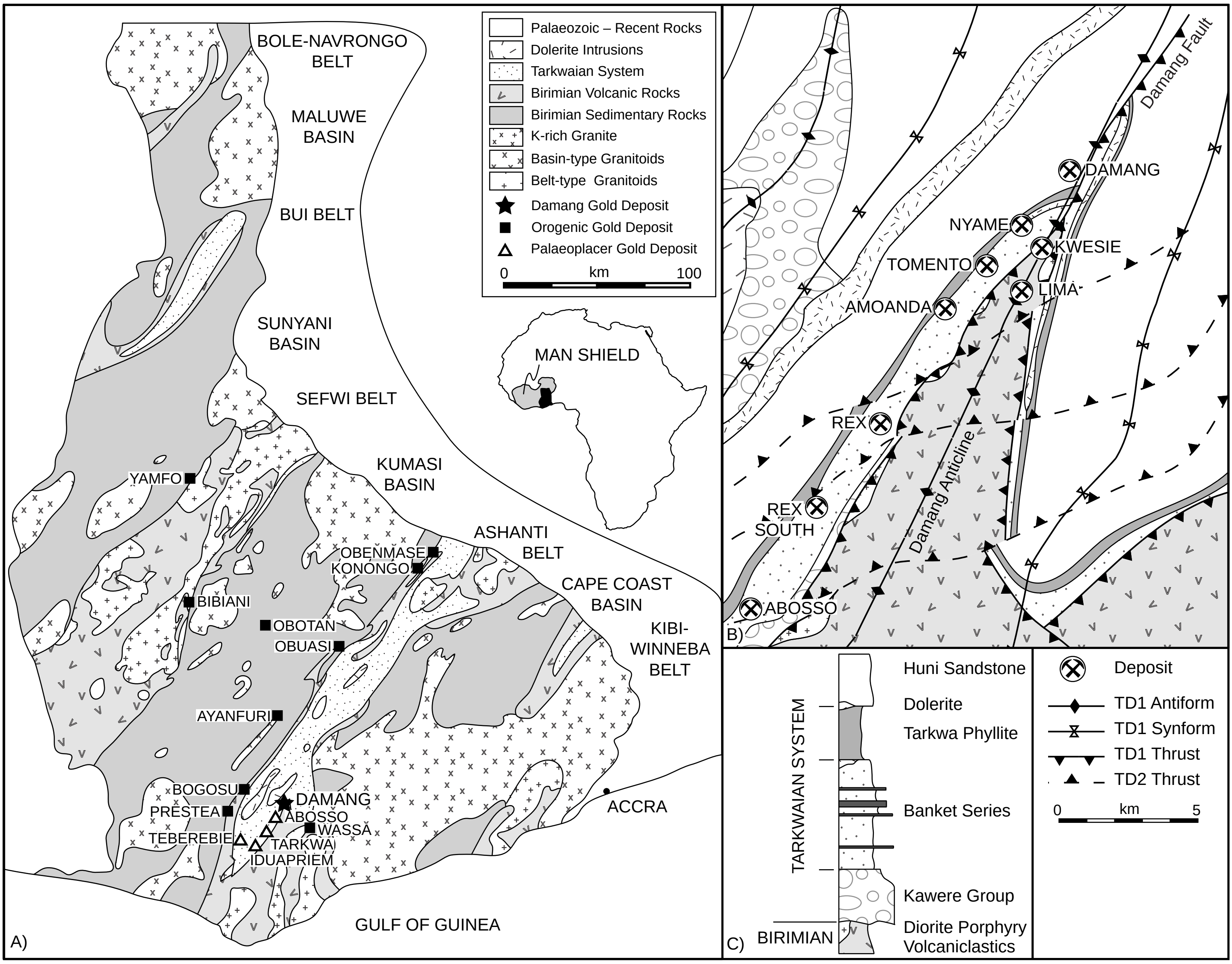

Palaeozoic – Recent Rocks
Dolerite Intrusions
Tarkwaian System
Birimian Volcanic Rocks
Birimian Sedimentary Rocks
K-rich Granite
Basin-type Granitoids
Belt-type Granitoids
Damang Gold Deposit
Orogenic Gold Deposit
Palaeoplacer Gold Deposit
0 km 100
BOLE-NAVRONGO BELT
MALUWE BASIN
BUI BELT
SUNYANI BASIN
SEFWI BELT
KUMASI BASIN
ASHANTI BELT
CAPE COAST BASIN
KIBI-WINNEBA BELT
MAN SHIELD
YAMFO
BIBIANI
OBOTAN
OBUASI
OBENMASE
KONONGO
AYANFURI
BOGOSU
PRESTEA
DAMANG
ABOSSO
WASSA
TEBEREBIE
TARKWA
IDUAPRIEM
ACCRA
GULF OF GUINEA
A)
Damang Fault
DAMANG
NYAME
KWESIE
TOMENTO
LIMA
AMOANDA
REX
REX SOUTH
ABOSSO
Damang Anticline
B)
Huni Sandstone
Dolerite
Tarkwa Phyllite
Banket Series
Kawere Group
Diorite Porphyry Volcaniclastics
TARKWAIAN SYSTEM
BIRIMIAN
C)
Deposit
TD1 Antiform
TD1 Synform
TD1 Thrust
TD2 Thrust
0 km 5


2m

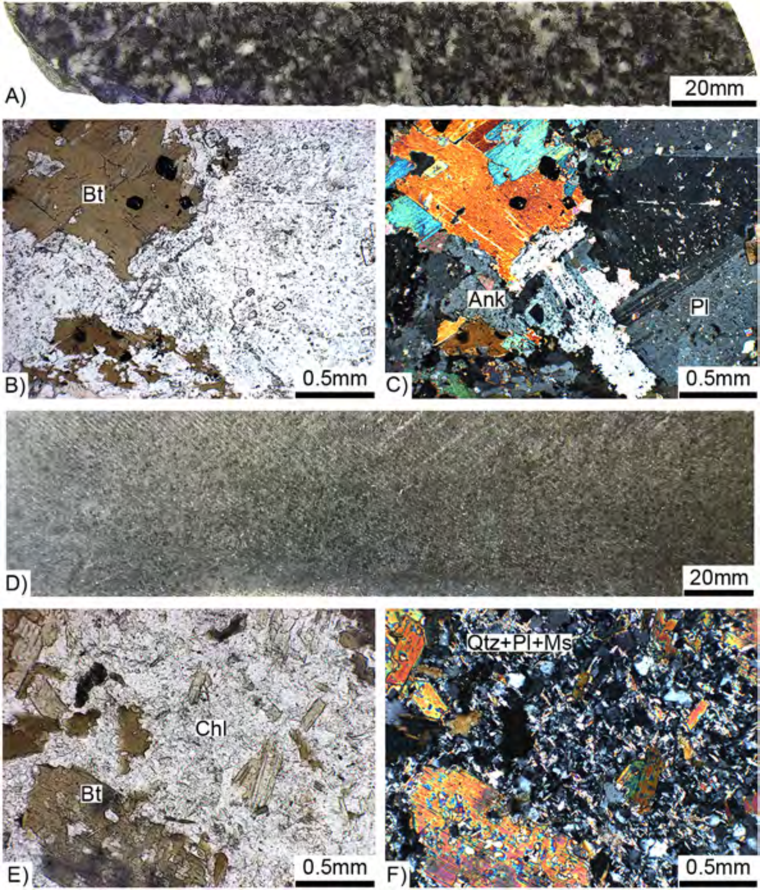
A)
20mm
B)
Bt
0.5mm
C)
Ank
Pl
0.5mm
D)
20mm
E)
Chl
Bt
0.5mm
F)
Qtz+Pl+Ms
0.5mm

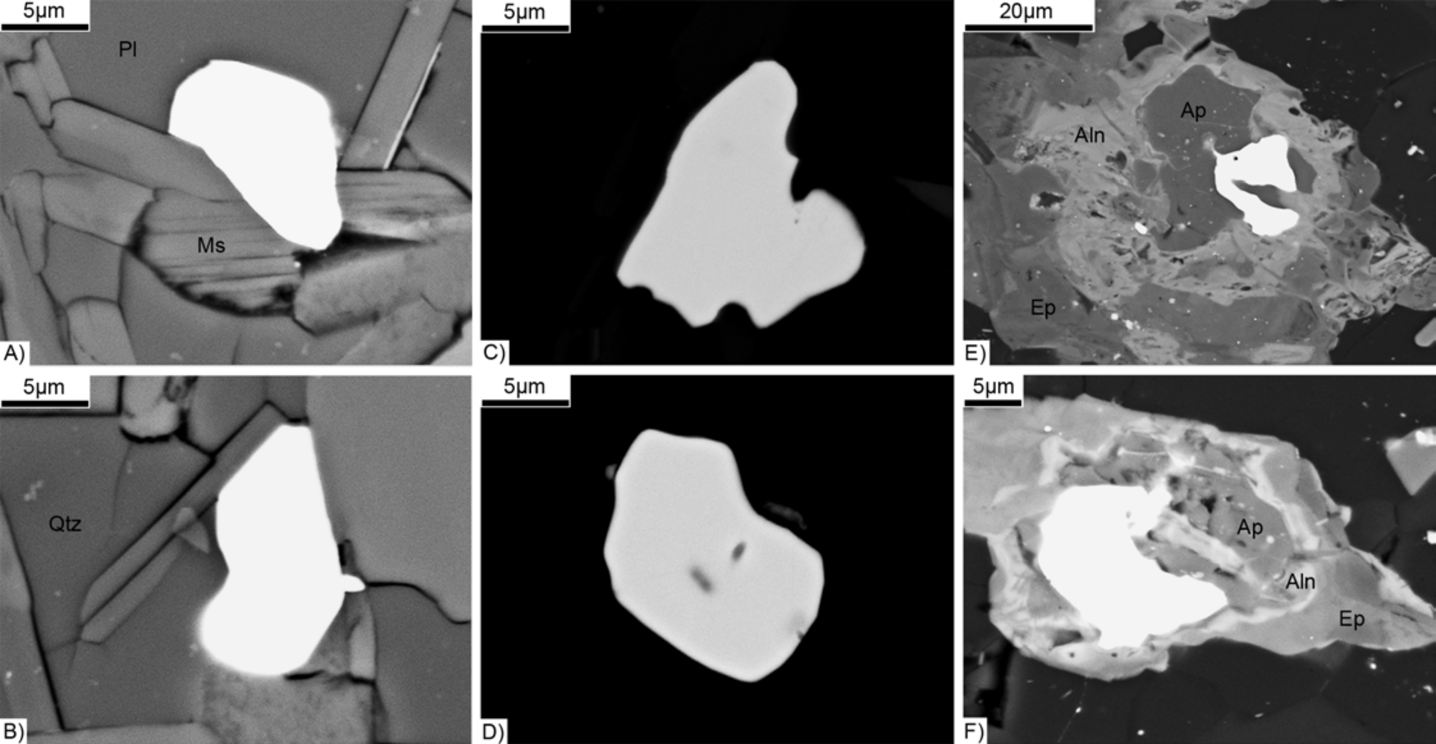

5µm
Pl
Ms
A)
5µm
Qtz
B)
5µm
C)
5µm
D)
20µm
Aln
Ap
Ep
E)
5µm
Ap
Aln
Ep
F)

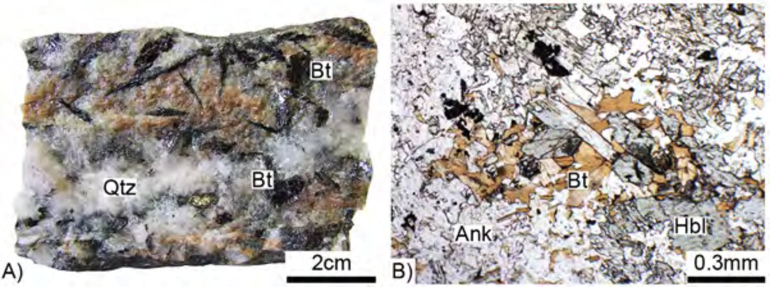
Bt
Qtz
Bt
2cm
A)
B)
Bt
Ank
Hbl
0.3mm

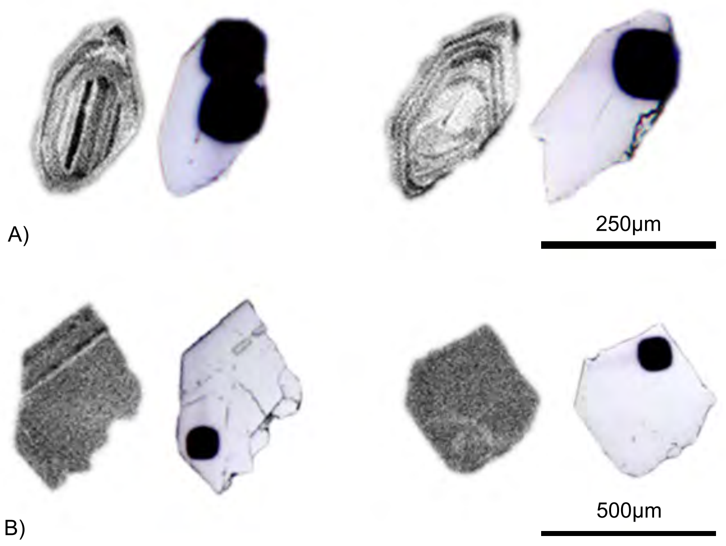
A)
250µm
B)
500µm

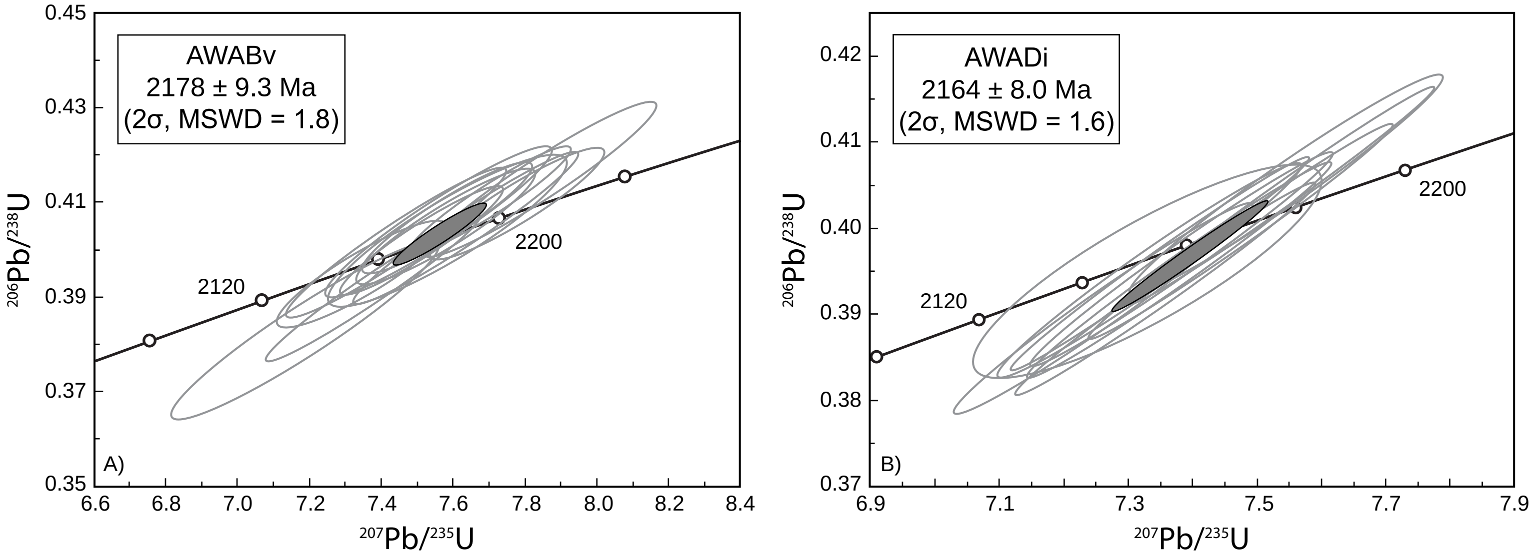
AWABv
2178 ± 9.3 Ma
(2σ, MSWD = 1.8)
A)
2120
2200
0.45
0.43
0.41
0.39
0.37
0.35
6.6
6.8
7.0
7.2
7.4
7.6
7.8
8.0
8.2
8.4
206Pb/238U
207Pb/235U
AWADi
2164 ± 8.0 Ma
(2σ, MSWD = 1.6)
B)
2120
2200
0.42
0.41
0.40
0.39
0.38
0.37
6.9
7.1
7.3
7.5
7.7
7.9
206Pb/238U
207Pb/235U

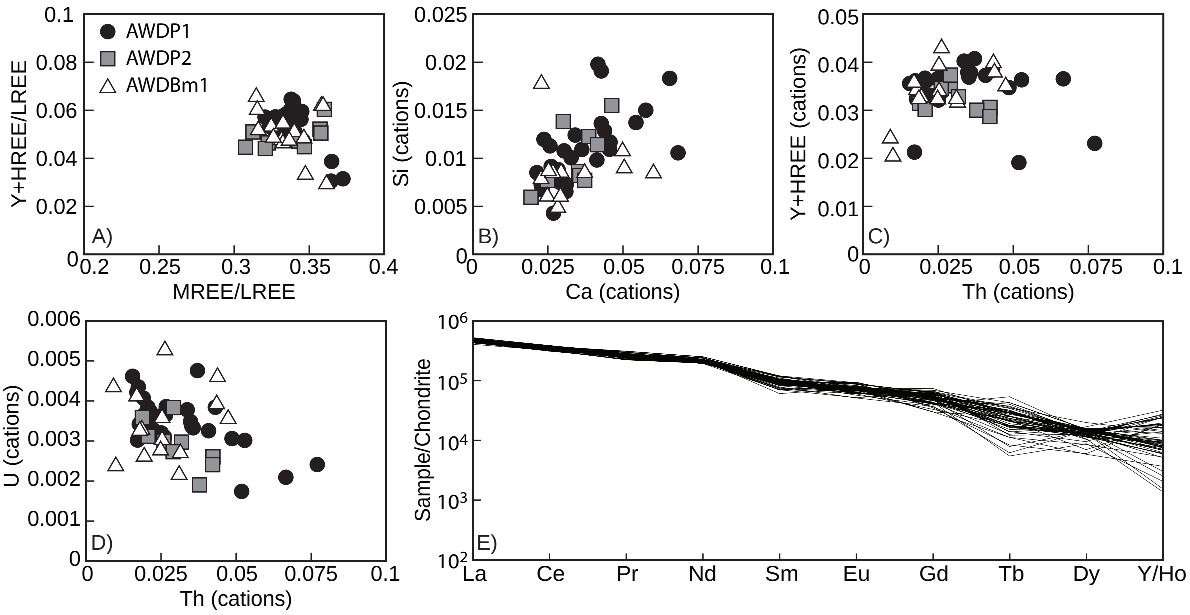
AWDP1
AWDP2
AWDBm1
Y+HREE/LREE
MREE/LREE
A)
Si (cations)
Ca (cations)
B)
Y+HREE (cations)
Th (cations)
C)
U (cations)
Th (cations)
D)
Sample/Chondrite
E)
La
Ce
Pr
Nd
Sm
Eu
Gd
Tb
Dy
Y/Ho

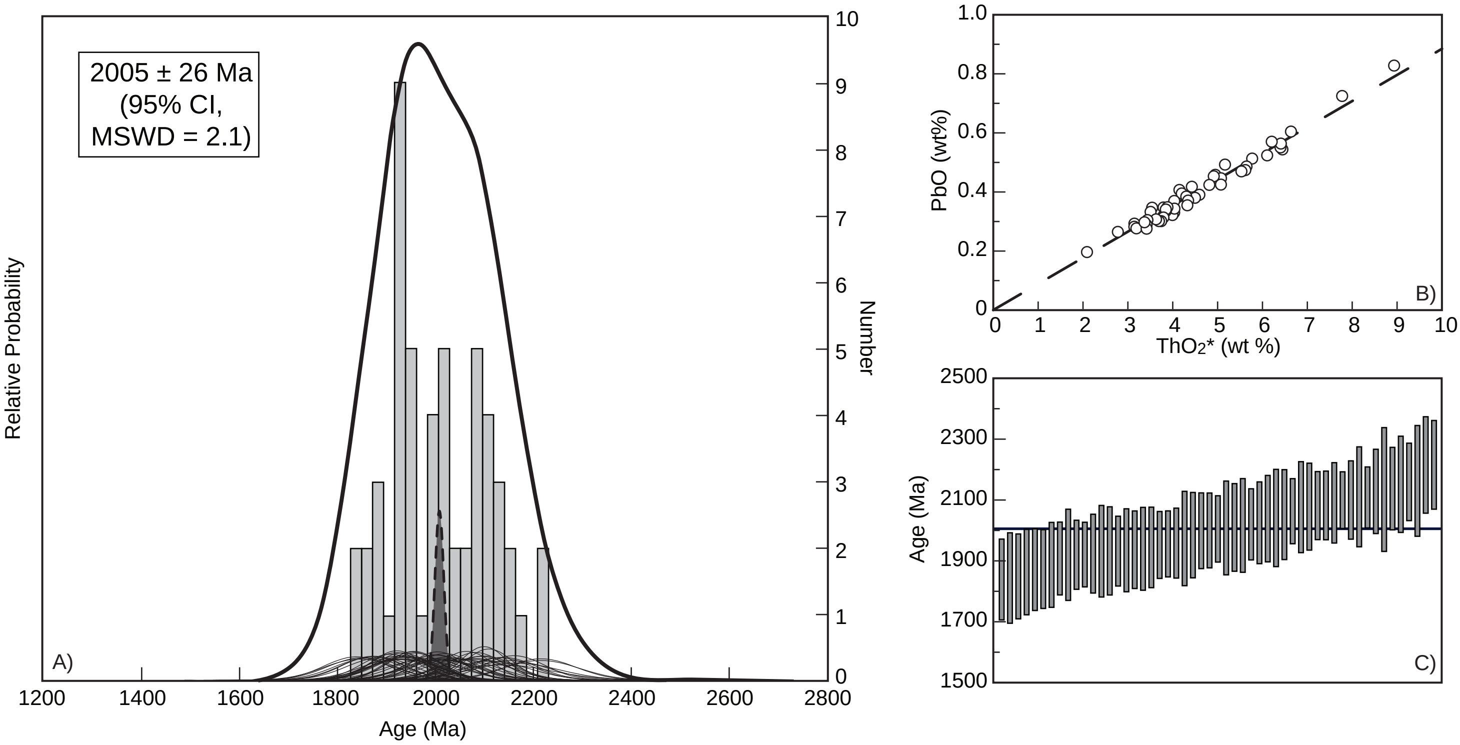

2005 ± 26 Ma
(95% CI,
MSWD = 2.1)
Relative Probability
Number
Age (Ma)
A)
PbO (wt%)
ThO2* (wt %)
B)
Age (Ma)
C)

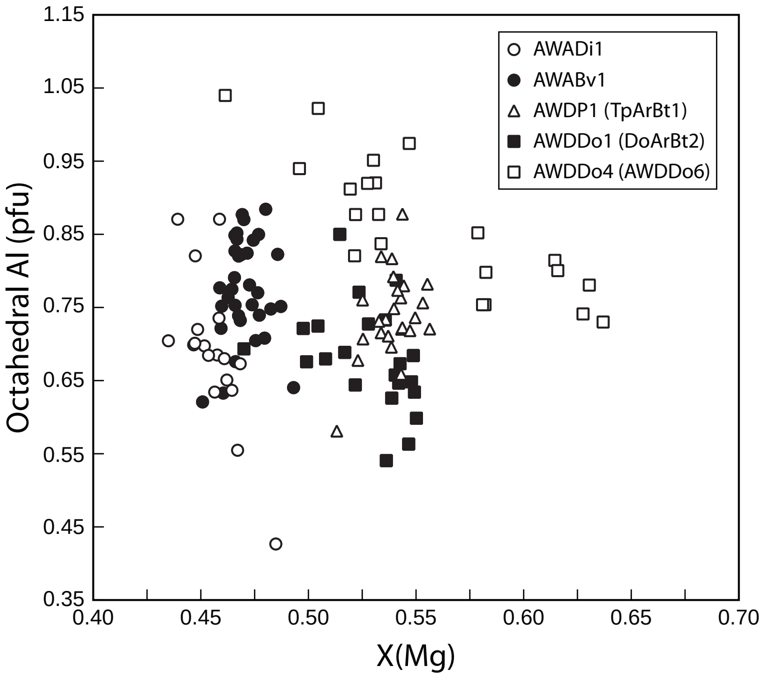

AWADi1
AWABv1
AWDP1 (TpArBt1)
AWDDo1 (DoArBt2)
AWDDo4 (AWDDo6)
Octahedral Al (pfu)
1.15
1.05
0.95
0.85
0.75
0.65
0.55
0.45
0.35
0.40
0.45
0.50
0.55
0.60
0.65
0.70
X(Mg)

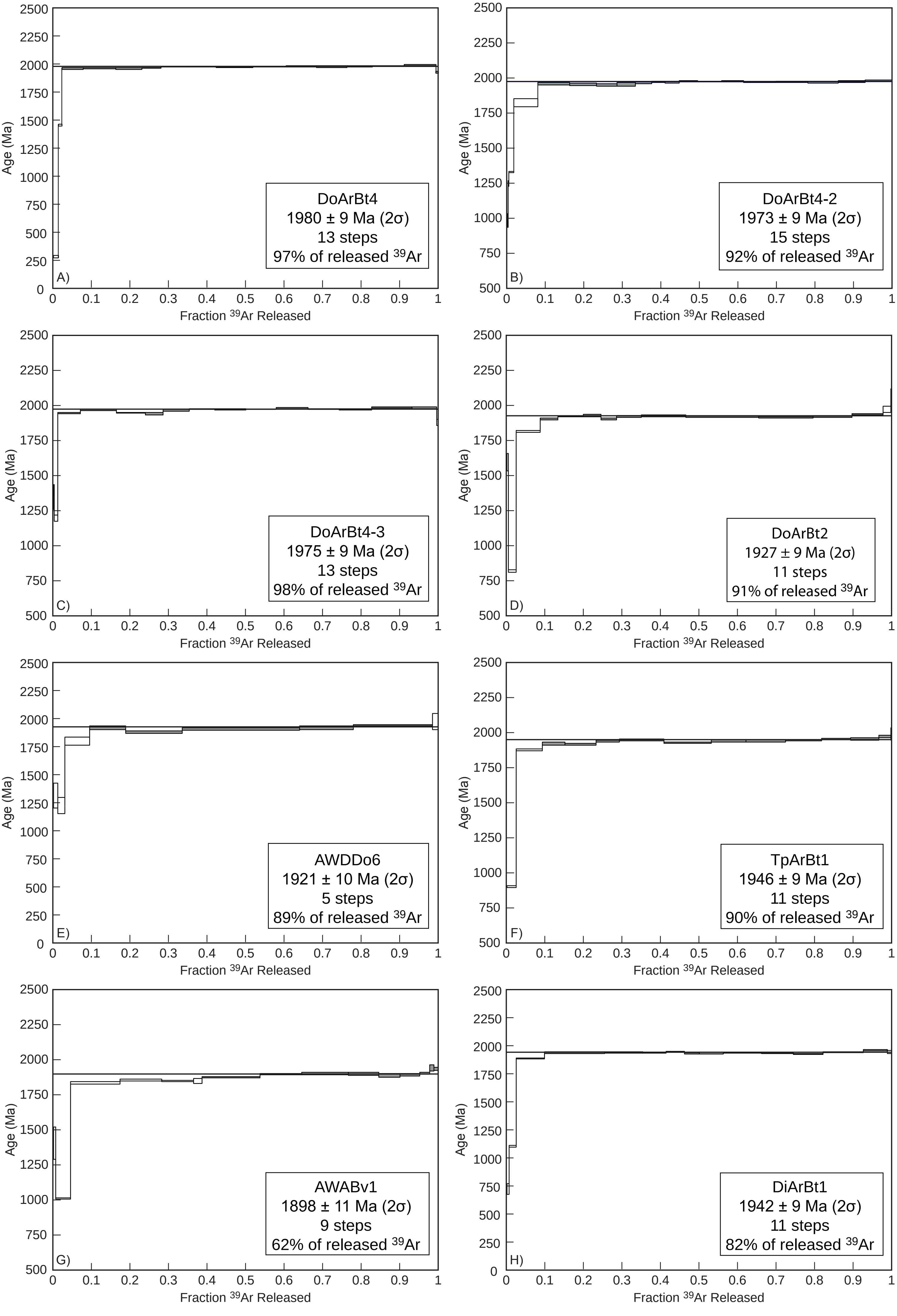
DoArBt4
1980 ± 9 Ma (2σ)
13 steps
97% of released 39Ar
A)
DoArBt4-2
1973 ± 9 Ma (2σ)
15 steps
92% of released 39Ar
B)
DoArBt4-3
1975 ± 9 Ma (2σ)
13 steps
98% of released 39Ar
C)
DoArBt2
1927 ± 9 Ma (2σ)
11 steps
91% of released 39Ar
D)
AWDDo6
1921 ± 10 Ma (2σ)
5 steps
89% of released 39Ar
E)
TpArBt1
1946 ± 9 Ma (2σ)
11 steps
90% of released 39Ar
F)
AWABv1
1898 ± 11 Ma (2σ)
9 steps
62% of released 39Ar
G)
DiArBt1
1942 ± 9 Ma (2σ)
11 steps
82% of released 39Ar
H)
Age (Ma)
Fraction 39Ar Released

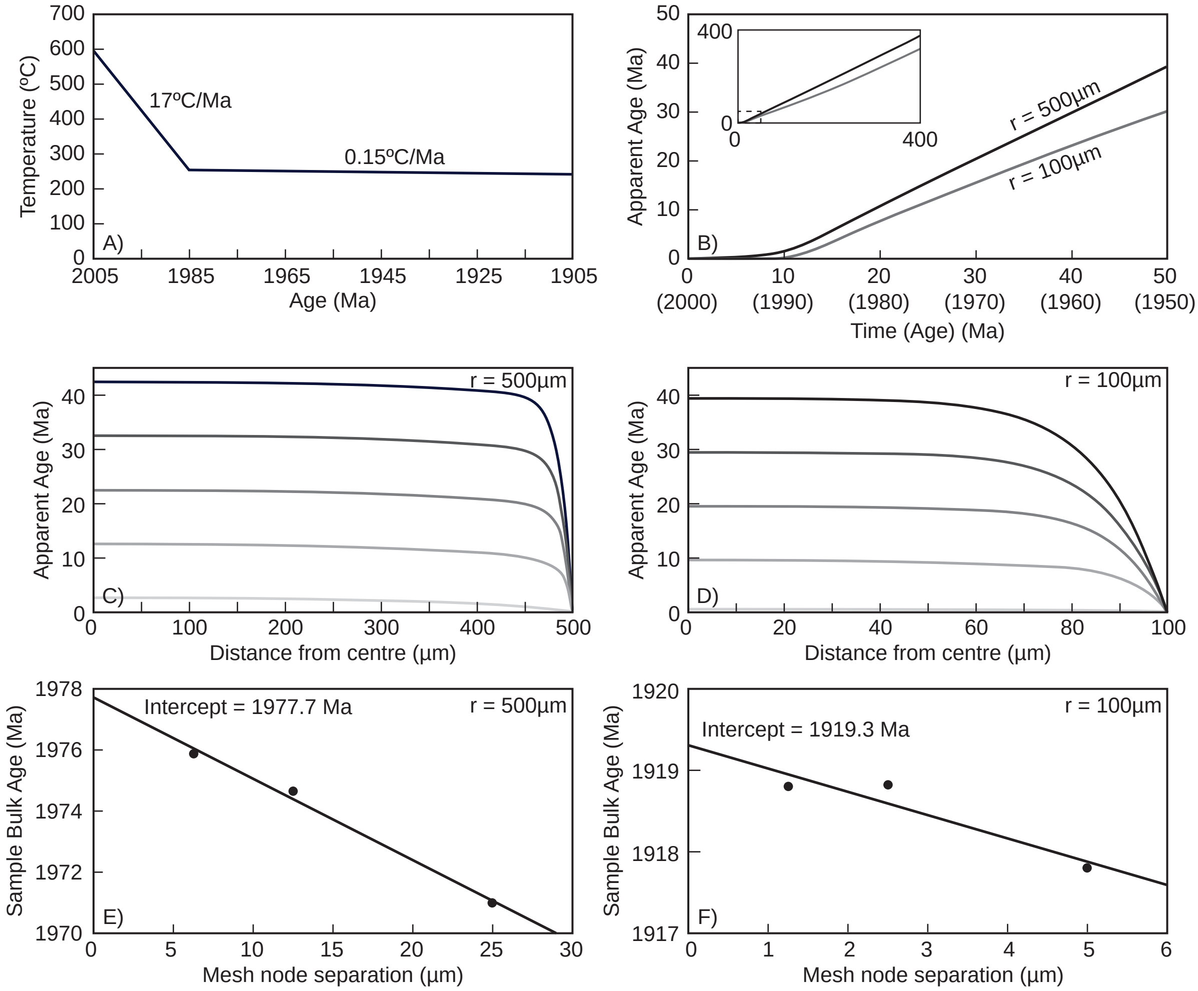

A)
Temperature (ºC)
Age (Ma)
17ºC/Ma
0.15ºC/Ma
B)
Apparent Age (Ma)
Time (Age) (Ma)
r = 500µm
r = 100µm
C)
r = 500µm
Apparent Age (Ma)
Distance from centre (µm)
D)
r = 100µm
Apparent Age (Ma)
Distance from centre (µm)
E)
Intercept = 1977.7 Ma
r = 500µm
Sample Bulk Age (Ma)
Mesh node separation (µm)
F)
Intercept = 1919.3 Ma
r = 100µm
Sample Bulk Age (Ma)
Mesh node separation (µm)

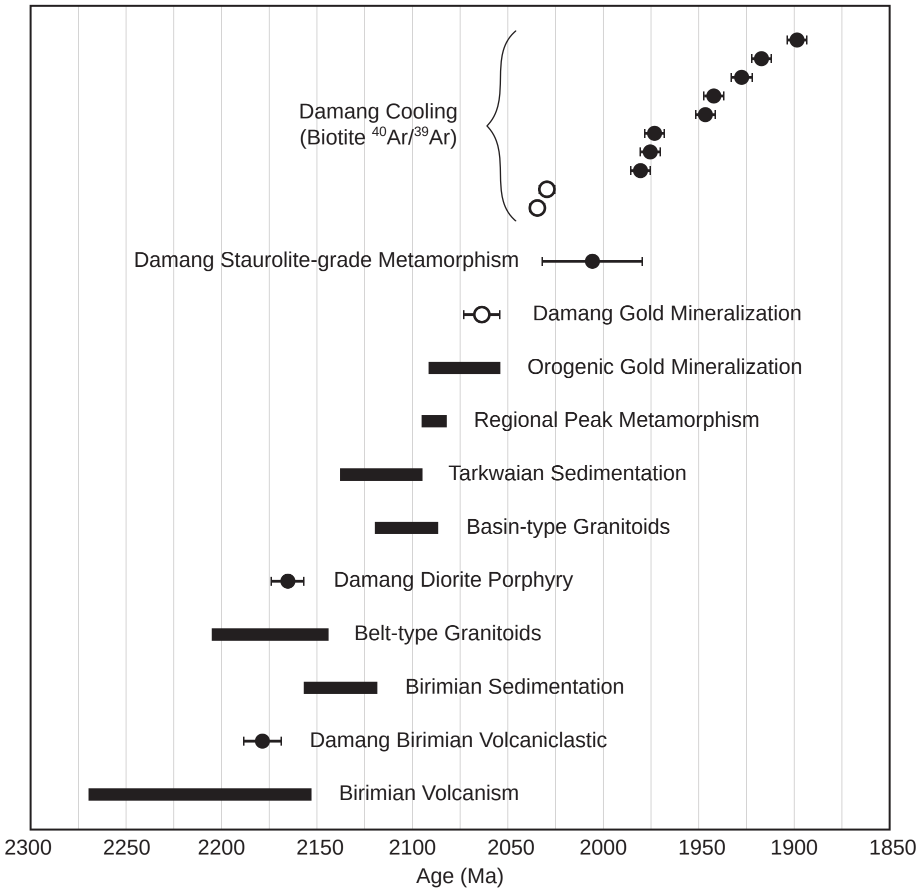
Damang Cooling
(Biotite $^{40}Ar/^{39}Ar$)
Damang Staurolite-grade Metamorphism
Damang Gold Mineralization
Orogenic Gold Mineralization
Regional Peak Metamorphism
Tarkwaian Sedimentation
Basin-type Granitoids
Damang Diorite Porphyry
Belt-type Granitoids
Birimian Sedimentation
Damang Birimian Volcaniclastic
Birimian Volcanism
2300
2250
2200
2150
2100
2050
2000
1950
1900
1850
Age (Ma)

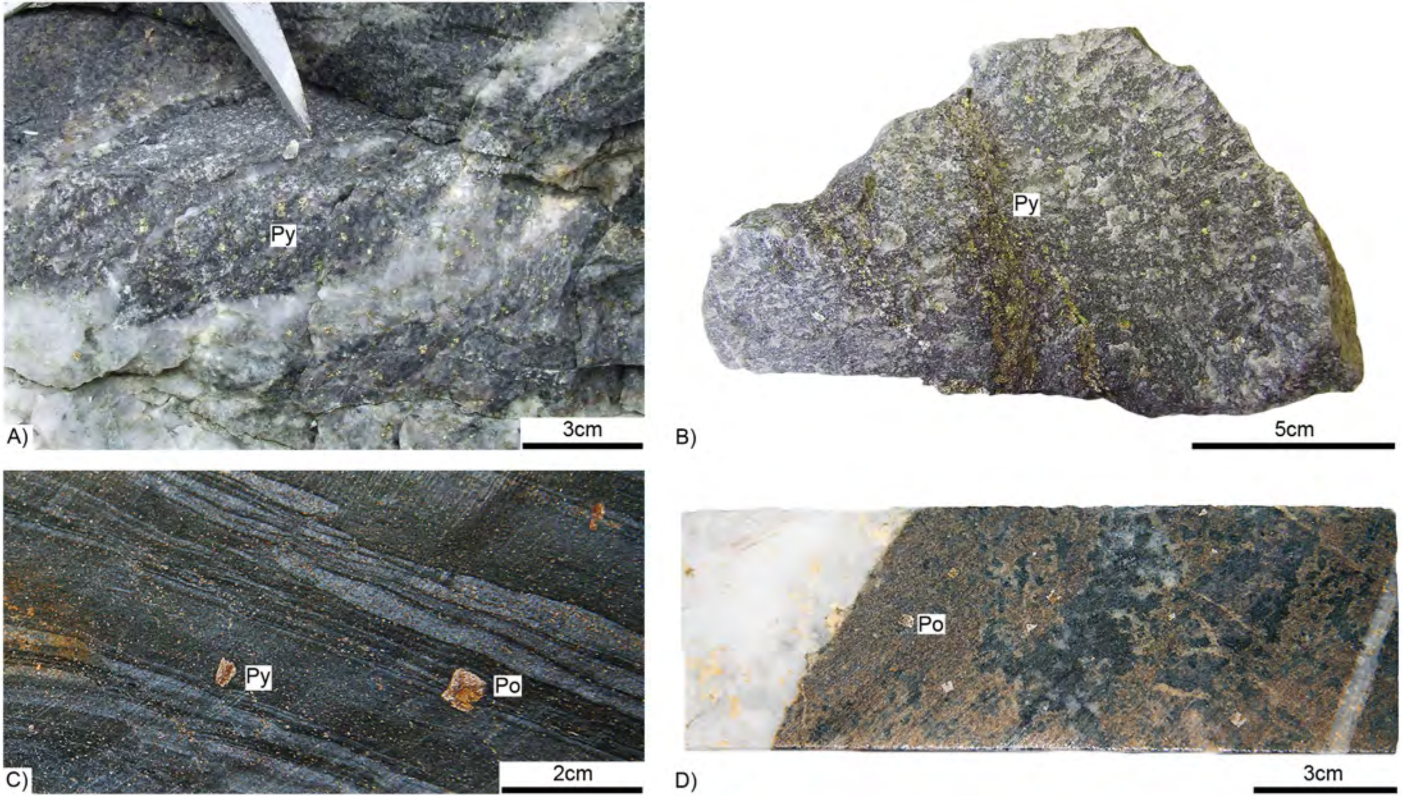
A)
Py
3cm
B)
Py
5cm
C)
Py
Po
2cm
D)
Po
3cm

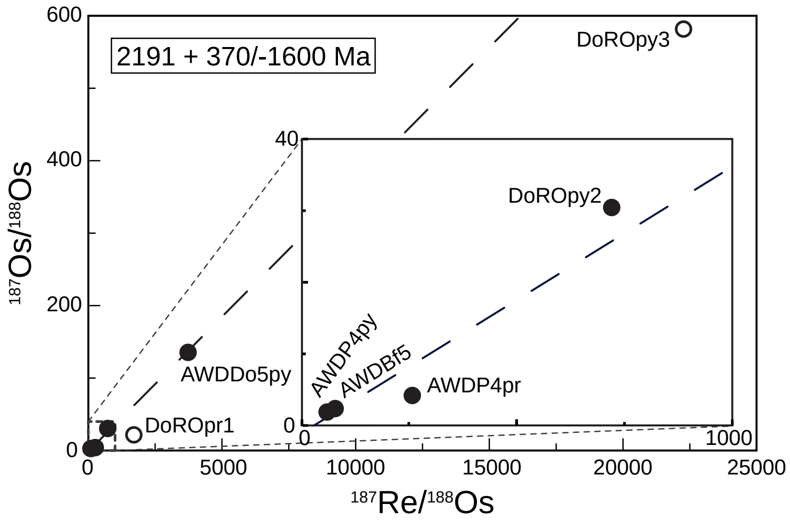

2191 + 370/-1600 Ma
DoROpy3
DoROpy2
AWDP4py
AWDBf5
AWDP4pr
AWDDo5py
DoROpr1
600
400
200
0
40
0
0
1000
0
5000
10000
15000
20000
25000
$^{187}Os/^{188}Os$
$^{187}Re/^{188}Os$